



**HAL**  
open science

## Micromechanics of primary creep in Ni base superalloys

Hyung-Jun Chang, Fivel Marc, Jean-Loup Strudel

► **To cite this version:**

Hyung-Jun Chang, Fivel Marc, Jean-Loup Strudel. Micromechanics of primary creep in Ni base superalloys. *International Journal of Plasticity*, 2018, 108, pp.21-39. 10.1016/j.ijplas.2018.04.009 . hal-01845076

**HAL Id: hal-01845076**

**<https://hal.science/hal-01845076>**

Submitted on 22 Dec 2020

**HAL** is a multi-disciplinary open access archive for the deposit and dissemination of scientific research documents, whether they are published or not. The documents may come from teaching and research institutions in France or abroad, or from public or private research centers.

L'archive ouverte pluridisciplinaire **HAL**, est destinée au dépôt et à la diffusion de documents scientifiques de niveau recherche, publiés ou non, émanant des établissements d'enseignement et de recherche français ou étrangers, des laboratoires publics ou privés.

# Micromechanics of primary creep in Ni base Superalloys

Hyung Jun CHANG<sup>1</sup>, Marc C. FIVEL<sup>2</sup> and Jean-Loup STRUDEL<sup>3</sup>

<sup>1</sup>Safran Tech, Rue des Jeunes Bois - Châteaufort, - 78772 Magny-Lès-Hameau, France

<sup>2</sup>Science and engineering of materials and processes, SIMAP, Univ. Grenoble Alpes/ CNRS, BP46, 38402, Saint-Martin d'Hères, France

<sup>3</sup>Centre des Matériaux, Mines-ParisTech-CNRS UMR 7633 BP 87-91003 EVRY Cedex, France

## Abstract

The initial stages of creep in nickel base superalloy deserve a special attention since they prevail in most of the service life of critical jet engine components. In nickel base superalloys, a very sharp minimum in creep rate is observed at strains less than 0.5% in a wide range of temperatures: the lower the applied stress the steeper the minimum, often referred to as incubation period. In this paper, the primary creep stage of Ni superalloy is investigated using 3D discrete dislocation dynamics modeling. The simulated volume corresponds to a 3D periodic cell of the cubic arrangement of  $\gamma$ - $\gamma'$  Ni-Al loaded along the (001) direction. Misfit stresses induced by the lattice mismatch ( $\delta = -3.10^{-3}$ ) between the precipitate and the matrix are taken into account through a coupling of the dislocation dynamics code with a finite element code. Frank-Read sources are positioned in the horizontal channel. It is shown that most of the dislocations propagate in the horizontal channels by repeated cross-slip on activated {111} glide planes and a few invade the vertical channels. This behavior is rationalized by the model. In the  $\gamma$ - $\gamma'$  interfaces, the zigzagging lines of dislocations straighten out into [100] and [010] directions leading to a dislocation microstructure similar to the ideal misfit dislocation network needed to compensate the lattice mismatch. Calculations of internal stresses in the channels show that this dislocation microstructure induces biaxial planar stresses in the horizontal  $\gamma$  channels leading to an elastic contraction of the sample along the loading direction. Three-dimensional DDD simulations show that the plastic strain induced, in the loading direction, by the movement and multiplication of dislocations is less important than the elastic relaxation it produces along that same direction. Hence, for very low applied tensile stresses, Ni superalloys display an abnormal behavior often referred to as negative creep that can be evidenced experimentally, even in polycrystalline materials. This last observation clearly implies that the first active batches of dislocations, during creep, or static high temperature ageing are mobilized to cancel out the numerous and pervading internal elastic strain fields generated within the crystals by the  $\gamma'$  precipitates due to their misfit with the  $\gamma$  matrix.

## 1. Introduction

Nickel base superalloys, hardened by large volume fractions of  $\gamma'$  precipitates, exhibit an outstanding creep resistance at elevated temperatures (400°C to 1150°C) under large stresses and for extended periods of time; therefore, they are commonly used in the hottest parts of aero-engines, as well as in land turbines. In advanced disk alloys the  $\gamma'$  volume fraction can reach 40 to 50% and in alloys designed for single crystal turbine blades 70%. In most nickel base superalloys the  $\gamma$ - $\gamma'$  misfit, defined as  $\delta = \frac{a_{\gamma'} - a_{\gamma}}{\bar{a}}$ , is negative and takes values as large as  $-3 \cdot 10^{-3}$ ; it varies widely ( $\pm 2 \cdot 10^{-3}$ ) with the chemical composition of the alloy (Pyczak et al. 2005, 2009) and the temperature (Lu et al., 2008; Royer et al, 1995) and, more subtly, with plastic strain and internal stress fields as pointed out by Kuhn et al. (1991) and experimentally measured with great details by Dirand et al. (2013).

The tensile and creep behavior of superalloys has been abundantly studied in a large range of temperatures and stresses; results and interpretations are reviewed in a number of articles (Pollock and Field 2002, Pope and Ezz 1984 most comprehensive and also Link et al., 2009, Zhang et al., 2005, Viswanathan et al., 2005). Yet, the rather peculiar primary creep stage they all exhibit, and its interpretation still need to be clarified. The objective of this work is to present an interpretation of experimental observations based on a micromechanical model combining a FEM approach to describe the local stress and strain fields around  $\gamma'$  precipitates, with a DDD approach to account for the dislocation activity. Thus, the movements of individual dislocation segments moving in the  $\gamma$  matrix, within these stress fields and in mutual interaction with their updated values can be described, as plasticity progresses during the initial stages of creep.

Primary creep, the stage that immediately follows the loading of the test piece is usually described as a stage of decreasing strain rate, until a steady state regime, characterized by  $\dot{\epsilon}(t) \approx cte$ , is reached (blue curve, Fig. 1). Instead, in nickel base superalloys (Fig. 1), a very sharp minimum strain rate is observed at around  $2$  to  $5 \cdot 10^{-3}$  strain, followed by a steep rise; then creep is progressively turning into a slowly accelerating stage that eventually merges into tertiary creep and rupture.

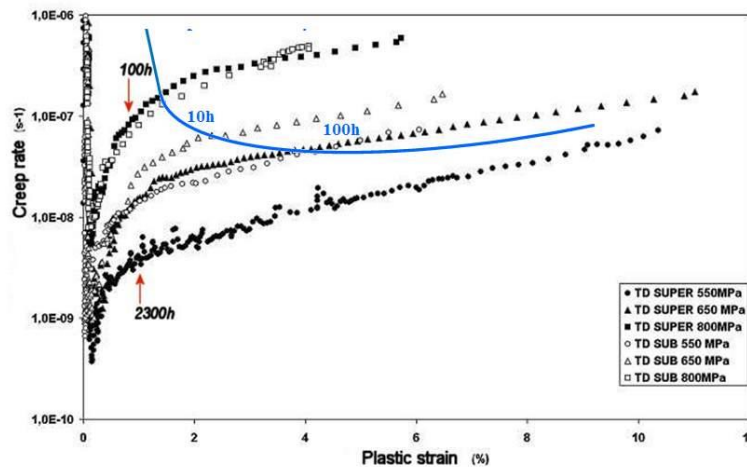


Fig. 1: Creep rate of René 88 at 700°C (Augustins-Lecallier, 2012).

This peculiar creep behavior, although already reported in the 90's by Provendier-Aubourg and Strudel (1995), who studied the creep and relaxation behavior at 650° C of alloy N-18, was improperly related to the formation of stacking faults developing in the matrix and extending into the  $\gamma'$  precipitates. At that time, these mechanical tests were performed at a rather low temperature and under high stresses (850 to 1000 MPa) in an alloy with high cobalt content (15.7 at %). The TEM observations were then biased by the overwhelming presence of stacking faults, and the role of perfect dislocations, located in the  $\gamma$ - $\gamma'$  interfaces, was screened by this abundance. Furthermore, the appropriate simulation tools that would have led to the correct interpretation were missing. Later, this marked minimum creep rate was observed in all superalloys containing a misfitting  $\gamma'$  phase (Epishin and Link, 2004a-b, Pyczak et al., 2005, Wu et al., 2016). Its amplitude seems to be increasing with the volume fraction of precipitates. It has been reported in AM1 (Fredholm and Strudel, 1988), in the CMSX series (Matan et al., 1989, Reed et al., 1999; Svoboda and Lukáš, 1998), in SRR 99 (Hammer and Mughrabi, 1989) in RR-1000 (Hardy et al., 2004), in René 88 (Fig. 1) and even in Alloy 800H under low stress, which contains only 2% volume fraction of  $\gamma'$  precipitates (El-Hazim, 1996). In CMSX 4 (Fig. 2), this sharp minimum creep rate was reported for  $\langle 001 \rangle$  oriented crystals tested at 1200° C under 75 and 50 MPa with strain rates in the range  $10^{-7}$  to  $10^{-9}$  s $^{-1}$ . Under such conditions, even in a low stacking fault energy alloy such as CMSX 4, perfect matrix dislocations alone are observed moving in matrix channels normal to the applied stress, by a repeated cross slip mechanism, as described by Carry and Strudel (1975) (Fig. 3).

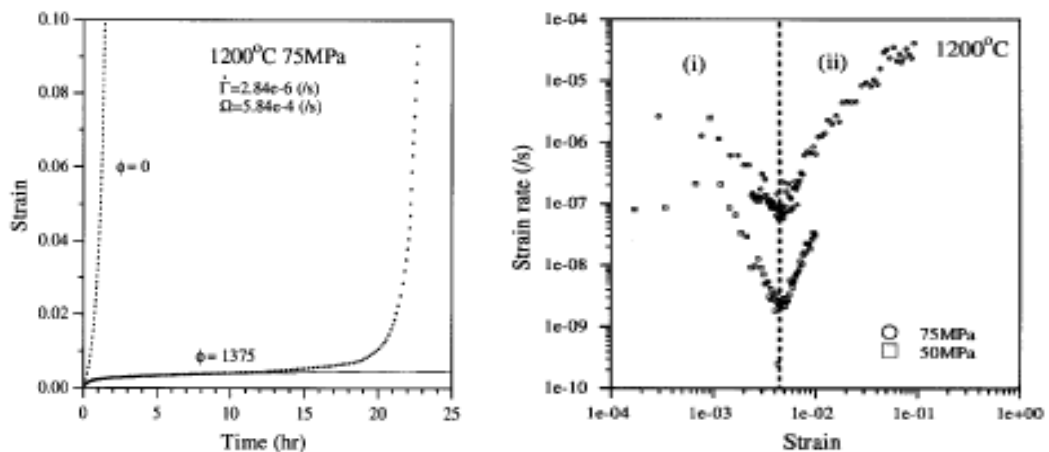


Fig. 2: Creep of CMSX-4 at 1200° C under low stress (Reed et al, 1999)

Notice that the originally zigzagging, mixed 60° lines left by the leading screw segment in the  $\gamma$ - $\gamma'$  interfaces, later straighten out into pure edge, straight lines oriented into the cube directions. Notice also that, on the average, the leading screw segments, by their repeated cross-slip behavior (Fig. 3), are moving in that same direction. Thus, it appears that the best conditions to observe and study this marked minimum creep rate is to submit a  $\langle 001 \rangle$  oriented single crystal to a tensile creep test, at fairly high temperature (750° C to 1200° C) under an applied stress, low enough to place that minimum creep rate around  $10^{-9}$  s $^{-1}$ , or below. It is difficult experimentally, to collect data so close to the background noise of the sensing and recording devices ( $10^{-10}$  s $^{-1}$  in a carefully air conditioned room) but this regime is actually most important, as it encompasses most service life or may even be considered as an upper bound to it. Indeed, the minimum creep rate under 75 MPa on the CMSX-4 test (Fig. 2), yields a value of  $6 \cdot 10^{-8}$  s $^{-1}$ . If we assume that this

minimum creep rate would be maintained for 45 hours, the material would already reach a plastic strain of 1%, an underestimated value, considering the assumption. In service, even for military engines, strain rates, at least, two orders of magnitude lower are usually required. Similarly, Ram et al. (2016), testing a high creep resistant single crystal at 900°C under 450 MPa report strain rates in the range  $\approx 10^{-8} \text{ s}^{-1}$  at 1% strain and a time to rupture of  $\approx 200 \text{ h}$ . As a consequence, they observe and model a scenario of general plasticity with dislocation avalanches affecting several families of channels simultaneously and involving interactions and junctions of dense populations of dislocations.

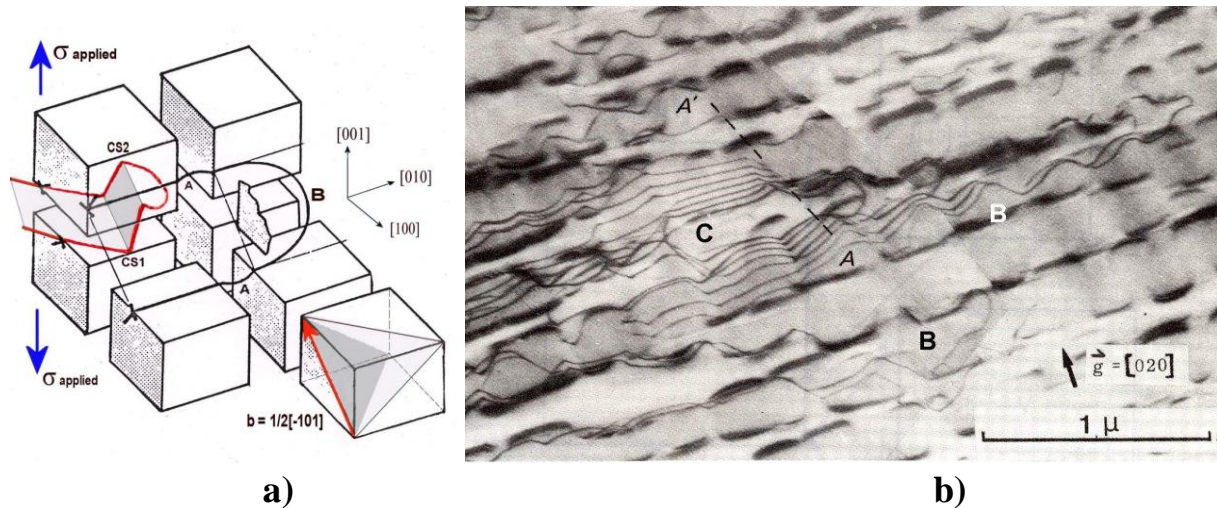


Fig. 3: Repeated cross-slip of the leading screw segment of a perfect dislocation leaving zigzagging  $60^\circ$  segments which straighten out along cube directions, by climb in the  $\gamma$ - $\gamma'$  interfaces. a) Schematic; b) TEM observation in alloy AM-1 at 850°C/ 190 MPa (Carry and Strudel, 1975).

Under high stresses, the details of the stress fields introduced by the  $\gamma$ - $\gamma'$  misfit need not be taken into account as shown by Huang et al. (2012), who simply introduced a uniform average internal stress field in each matrix channel where the multiple slip systems are crisscrossing and interacting with one another. They even claim that the coherency stress field has negligible influence on the stress-strain response of the material. Similarly, Rao et al. (2004), using a DDD simulation model to obtain an estimate of the yield stress of superalloys, indicate that, when introducing a coherency stress induced by a misfit  $\delta = -0.3\%$ , the yield stress increases by only about 10%.

In this paper, the dislocation configurations examined are those similar to service conditions; i.e. creep under intermediate and high temperature, under applied stresses low enough to produce rupture after several thousand hours and creep rates, after 1 % strain, 200 to 500 times lower than those previously described in the literature (Reed et al., 1999; Ram et al., 2016). When applied stresses are low, the local internal stress fields generated by precipitates or pre-existing dislocation arrangements must be taken into account when trying to understand the movement of dislocations. In nickel base superalloys, the misfitting  $\gamma'$  phase is generating nonuniform 3-D stress fields that strongly distort and pre-strain the matrix with an intensity increasing with the amplitude of the misfit, the volume fraction of precipitates and their morphology. A precise 2D-mapping of the stress field surrounding  $\gamma'$  cuboids was first published by Pollock and Argon (1992) and more recently in 3-D by Link et al. (2009), who could thus

identify and localize specific edges of cuboids where the presence of particular stress components are favoring the repeated cross slip of dislocations moving in a quasi-periodic array of cuboids of identical size (Fig. 4a). The first part of this paper will be devoted to the presentation of the 3D stress field and its variations along and across the three matrix channels, 1) in the absence of any applied stress and 2) under a uniaxial tensile stress along  $\langle 001 \rangle$ . Then the resolved shear stress for a given slip system, instead of the Von Mises stress, will be calculated in a FEM scheme.

When a perfectly oriented  $\langle 001 \rangle$  single crystal is submitted to a tensile stress, four different Burgers vectors are expected to be active simultaneously. In practice, single crystals exhibit a mosaic structure and only one or two dislocation systems are activated simultaneously in any given subgrain. If the disorientation happens to be toward  $[011]$  for instance, the two activated Burgers vectors are orthogonal, i.e.  $a/2[101]$  and  $a/2[-101]$  and the dislocations have little interaction with each other; on the other hand, if the disorientation happens to be toward a  $\langle 111 \rangle$  direction, the two activated Burgers vectors, i.e.  $a/2[101]$  and  $a/2[011]$  share a common glide plane, namely  $(111)$ , where they can recombine to form  $a/3[11-2]$  configurations that can shear the  $\gamma'$  particles by creation of low energy superlattice intrinsic and extrinsic stacking faults (Kear et al., 1970). As reported by Wu et al (2016) and at length by Rae and Reed (2007), such complex events can take place during primary creep of superalloys with low stacking faults energy (CMSX-4, for instance) and produce a second creep rate minimum around 4 to 5% strain (Svoboda and Lukáš, 1998). In fact, it is necessarily preceded by the generation of perfect matrix dislocations moving in the  $\gamma$  matrix channels and interacting with the internal stress field. As described above, they are responsible for the first minimum. Only then, can the various perfect dislocations recombine into complex planar slip systems involving planar defects. In this paper, this second stage of primary creep will not be examined since it has been well described and interpreted at length by several authors (Unocic et al., 2008; Rae and Reed, 2007; Knowles and Chen, 2003; Rae et al., 2001) and is taking place only under applied stresses high enough for the penetration and shearing of  $\gamma'$  precipitates to take place.

In situ measurements of  $\gamma$  and  $\gamma'$  lattice parameters during monotonic tensile tests, at temperature, were made by use of neutron diffraction techniques and their variations were interpreted as “load transfers” between the matrix and the precipitates in a PM version of RR1000 (Preuss et al., 2008), as well as in the DS-MAR-M200 (Lu et al., 2008) alloys. Making use of an ingenious experimental set-up for carrying out tensile creep tests at 900°C and above, Lu et al. (2008) clearly established that a significant reduction of the elastic strain of the  $\gamma$  matrix channels along the tensile direction was taking place during the first 10 hours of creep at 900°C under 425 MPa, on a DS MAR-M200 sample, while it was increasing in the transverse direction. The authors correctly attributed these “load transfers” between the  $\gamma$  matrix and the  $\gamma'$  cuboids to the presence of dislocations in the  $\gamma$ - $\gamma'$  interfaces relaxing the misfit generated elastic strain fields in the channels normal to the applied uniaxial stress and, on the other hand, aggravating them in the longitudinally oriented channels. But they omitted to take into account the effect of the misfit stresses when estimating the stress necessary for matrix dislocations to bow out, into the matrix channels, assuming simply an Orowan process, hence a purely geometric effect. This latter case of interactions between dislocations and impenetrable spherical particles is relevant in ODS type materials and was recently treated with a theoretical approach and in a comprehensive manner by Zalezak et al. (2017).

The suggestion that the elastic relaxation of the pre-stressed matrix channels provided by the introduction of dislocations during the initial stages of plasticity could exceed the forward plastic strain produced by their generation and multiplication in the horizontal channels was first introduced by Strudel 2007. But the argument was purely qualitative; a quantitative estimate with appropriate tools is carried out here. The mechanisms of plasticity and the local stress redistributions in the presence of moving dislocations are examined quantitatively in the present paper; thus providing a tentative answer to the question of interaction between the plastic and elastic driving forces of the rafting phenomena in nickel base superalloys (Ichitsubo et al., 2003).

As pointed out by Fredholm et al. (1988) who studied the rafting process in AM-1 and more recently emphasized by Zhang et al. (2005; 2010), the movement, initially by glide and cross-slip, later by climb, together with the organization of dislocations into dense networks in the  $\gamma$ - $\gamma'$  interfaces of the horizontal channels are the precursor events of rafting of the  $\gamma$ - $\gamma'$  microstructure. These phenomena minimize the elastic strain energy initially stored in optimally heat treated superalloys (Ratel et al., 2010) and ensure a marked minimum creep rate for alloys with a large negative misfit (Zhang et al., 2005; Pyczak et al., 2009). Recently, Tanaka et al. (2011) pointed out that the initial elastically strained state of the  $\gamma$  matrix channels along the tensile direction  $\varepsilon_{33}$ , was drastically altered during the first stages of a uniaxial creep test. By use of the concept of eigenstrain of the  $\gamma$  matrix submitted to the stress resulting from the  $\gamma$ - $\gamma'$  misfit and to the plastic strain provided by creep, they show that the optimal resistance of the rafting  $\gamma$ - $\gamma'$  microstructure is obtained when the density of interfacial dislocations barely reaches the optimal value for which the misfit is globally balanced in the horizontal channels. It is one of the goals of this paper to suggest a rational and quantitative interpretation of this matrix stress relaxation based on the introduction of interfacial dislocations in preferential matrix channels under the applied stress, during the initial stages of plastic deformation.

Three dimensional Discrete Dislocation Dynamics (DDD) simulation is an ideal tool when investigating the initial stage of creep behavior of Ni base superalloys. Indeed, the amount of plastic strain and the size of the typical representative cell of an idealized single crystal of superalloy are both limited so that the required computation time is not too demanding. For this reason a few DDD simulations were conducted in 3D in the last few years. As an example, (Devincre et al. 2001; Vattré et al., 2009; Vattré et al., 2010) used a coupling with Finite Element (FE) to account for the misfit stresses and their Discrete-Continuum model was able to account for elastic anisotropy. They computed the creep behavior and the dislocation microstructure obtained under [001] and [111] tensile loading conditions (Vattré et al., 2010) and also the shearing process of the  $\gamma'$  precipitates (Vattré et al., 2009). Practically, most of the DDD simulations performed so far focused on the precipitate shearing process which corresponds to the creep behavior under high stress (Yashiro et al., 2006; Vattré et al., 2009; Huang et al., 2012; Yang et al., 2013; Li and Wang, 2014; Gao et al., 2015a-b; Gao et al 2017; Hussein et al., 2017). Consequently, only a few of them account for the misfit stresses, either using FEM (Devincre et al., 2001; Liu et al., 2014) or FFT approaches (Gao et al., 2015b).

Liu et al., 2014 were able to investigate the early stage of high-temperature low-stress creep in Ni-base superalloys using a DD framework where the misfit stress was implemented as an ad-hoc bi-axial stress field as also done by Huang et al., 2012. They focused their study on the motion of the interfacial dislocations and their local reactions at the  $\gamma$ - $\gamma'$  interface but nothing was said on the resulting mechanical response. Yashiro et al., 2008 also presented a DDD

investigation of the stability of the interfacial dislocation network and its interaction with a prismatic dislocation loop but they did not take into account the misfit stress. More recently, Ram et al., 2016 used ECCI observations to define arrangement of dislocations that served as the initial configuration of a DDD simulation. Neglecting the misfit stress, they observed how the dislocations could invade the different channels and they conclude that dislocation sources should exist somewhere outside the considered low-angle boundaries in order to account for the observed creep behavior. In the case of Ni-based superalloy with low stacking fault energy, Huang and Li, 2013 took into account dislocation dissociation in their DDD model to investigate the dislocation microstructure developed in the channels.

Thus, the aim of this paper is to use 3-dimensional DDD simulations in order to address the creep anomaly evidenced in the early stage of creep deformation of Ni superalloys, in two steps: first by computing, for a [001] oriented single crystal, the dislocation paths and resulting patterns, induced by the misfit stresses superimposed to a [001] tensile loading, typical of in service turbine blade conditions; secondly by estimating the elastic and plastic strain induced by the generation and multiplication of dislocations, belonging to one or several slip systems, getting trapped in the  $\gamma$ - $\gamma'$  interfaces where they climb and rearrange into straight lines along the cube directions. Finally, a stress analysis is conducted inside an ideal interfacial network aiming at perfectly compensating the misfit stress fields.

## 2. Simulation setup

### 2.1 Dislocation Dynamics modeling

The DD code used in this paper is the 3D edge-screw model TRIDIS as described in (Verdier et al., 1998). In this model, the dislocation lines are decomposed into sets of edge and screw segments connected together. The DD code is coupled to the Finite Element (FE) software CAST3M (CASTEM) in order to enforce complex boundary conditions. For each dislocation segment, the Peach Koehler force is computed at its middle point and projected along the glide direction. This effective force results from the superposition of the internal stress field generated by all the dislocation segments and the applied stress field obtained by the Finite Element correction. This gives the effective resolved shear stress,  $\tau^*$ , from which the dislocation velocity is evaluated as

$$v = \frac{\tau^* b}{B}, \quad [1]$$

where  $b$  is the Burgers vector magnitude and  $B$  is a phonon drag coefficient.

At high temperature, one should account for recovery mechanisms like cross-slip and eventually climb. In this paper, climb mechanism is not taken into account but cross-slip is implemented as proposed by many authors (Verdier et al., 1998)(Weygand et al. 2001)(Zbib and Diaz de la Rubia, 2002)(Kubin). In the case of screw segments, the cross-slip mechanism is computed via a thermally activated probabilistic algorithm aiming at modelling the constriction-expansion mechanism proposed by (Bonneville et al., 1988). First we compute the probability function,  $P$ , using the following formula

$$P = \alpha \frac{L}{L_0} \frac{\Delta t}{\delta t_0} \exp\left(\frac{\tau_{CS} - \tau_{III}}{kT/V}\right), \quad [2]$$

with  $L$  the dislocation length;  $\Delta t$  the waiting time;  $\tau_{CS}$  the shear stress resolved in the deviate slip system;  $\tau_{III}$  the critical shear stress at the onset of Stage-III hardening;  $T$ , the temperature and  $V$ , the activation volume.  $L_0$  and  $\delta t_0$  are reference length and time respectively and  $\alpha$  is a prefactor normalizing the range value of function  $P$  into  $[0;1]$  interval. At each time step, the value of  $P$  is compared to a computer generated random number,  $r$ , and the change of plane is accepted if  $r < P$ . The set of parameters used for the DDD simulations are given in Table 1.

b [Ang]	B [Pa.s]	$\alpha$	$L_0$ [ $\mu\text{m}$ ]	$\delta t_0$ [s]	$V/b^3$	$\tau_{III}$ [MPa]	$\delta t$ [s]	$\mu$ [MPa]	T [K]
2.54	$1.5 \cdot 10^{-5}$	$6 \cdot 10^4$	1.0	$10^{-9}$	350	200	$10^{-11}$	81000	800

Table1: Parameters used for DD simulations (Equ. (1) and (2)).

### 2.1 Geometry and boundary conditions

Assuming periodic boundary conditions, the elementary simulation box consists of a 500 nm cubic cell containing one horizontal channel and two vertical channels (Fig. 4). The channel thickness is fixed at 80 nm leading to a volume fraction of  $\gamma'$  precipitates of 59.3% with a precipitate size of 420 nm. Notice that only 1/8 of the volume of the 8  $\gamma'$  cuboids appears in Figure 4 since the center of the elementary box is chosen at the meeting point of the 3 matrix channels, in order to observe more easily the movement of dislocations in the matrix channels. In practice, periodic boundary conditions are enforced in the DD code by re-introducing dislocation segments in the opposite surface it escaped from. For each dislocation segment, the internal stress field is computed as if the segment was at the center of the periodic box. This means that the number of replicas taken into account for the dislocation stress field is  $N=1$ .

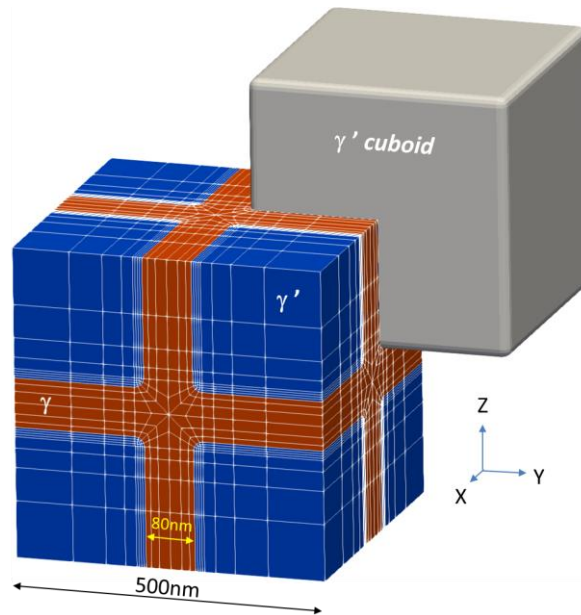


Figure 4: Geometry of the periodic simulation box and the corresponding finite element mesh used for the DD modelling. A typical  $\gamma'$  cuboid particle is superimposed to better illustrate the 3D geometry.

The entire volume is meshed into 6912 twenty-node elements (27873 nodes) locally refined at the  $\gamma$ - $\gamma'$  interface. In order to better represent the actual shape of the  $\gamma'$  precipitates, we designed cuboids with round corners of 15nm radius; they match closely the shapes predicted by phase field method (Gao et al., 2015a). The periodic boundary conditions in the FEM are enforced by imposing that the distance between two nodes belonging to two opposed surfaces is a constant throughout all the nodes of the face using CAST3M operator @CLPC.

Using the superposition principle, the dislocations are moving in the  $\gamma$  matrix according to an effective stress computed as the summation of the internal stress induced by all the dislocations included in the simulation box and the finite element stress accounting for the boundary conditions. Here the boundary conditions are of four types: (i) the misfit stress induced by the lattice mismatch between the  $\gamma$  matrix and the  $\gamma'$  precipitate; (ii) the load applied as a tensile stress along the [001] direction; (iii) the periodic boundary conditions along the (100), (010) and (001) surfaces of the simulated box and (iv) the non-penetrable facets located at the  $\gamma$ - $\gamma'$  interface.

Both the matrix and the precipitate are considered as elastic isotropic media with a Young modulus of  $E=208,000\text{MPa}$  and a Poisson's ratio  $\nu=0.3$  leading to a shear modulus  $G=80,000\text{MPa}$ . In this study, the difference in elastic moduli of the two phases is neglected so that the calculation of the image forces induced by the precipitate can be omitted. Practically, the presence of the precipitates is accounted for by the introduction of facets at the  $\gamma$ - $\gamma'$  interface which prevent the dislocations from entering the particles (Shin et al., 2003).

## 2.2 Dislocation configuration

After optimized heat treatments, the hardening phase with simple cubic ordered  $L1_2$  crystalline structure is generally arranged in nearly periodic arrays of cuboids,  $0.4\ \mu\text{m}$  in size, in quasi-coherency with the  $\gamma$  matrix and aligned along the  $\langle 001 \rangle$  cube directions (Fig. 3). The remaining  $\gamma$  channels of the fcc matrix are narrow ( $0.05$  to  $0.1\ \mu\text{m}$ ) and highly stressed by the misfitting cuboids they are surrounding. The  $\gamma$ - $\gamma'$  misfit parameter is of the order of  $-3.10^{-3}$  in many nickel base superalloys, a value usually considered as offering the best creep resistance (Pyczak et al., 2009).

Four dislocation sources are introduced as pinned segments of screw character located within the  $\gamma$ -matrix in the horizontal channel. Each screw segment is centered in the middle of the cuboid interfaces as shown in Figure 5. The initial length of each segment is set to  $86\ \text{nm}$ .

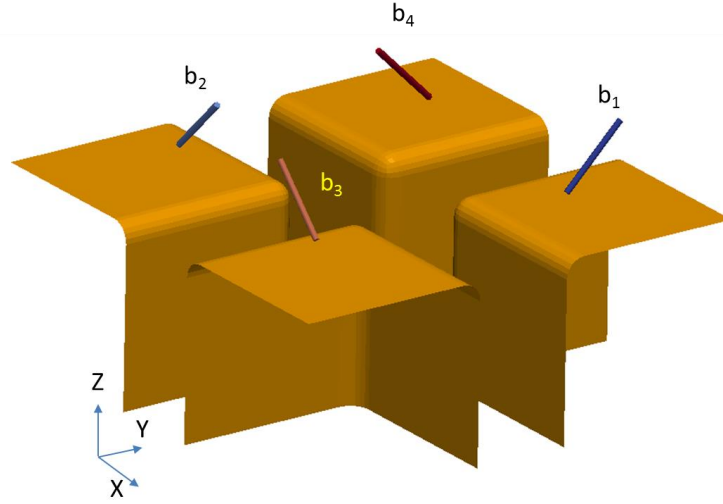


Figure 5: Initial dislocation configuration for the DD simulation and facet description. The upper part of the simulated box was removed for clarity.

The Burgers vectors of the 4 dislocations correspond to the 8 possible slip systems activated by the (001) loading i.e.:  $b_1=a/2$  [011],  $b_2=a/2$  [101],  $b_3=a/2$  [-101] and  $b_4=a/2$  [0-11], where  $a=3.52$  Å. Since each dislocation segment is artificially pinned at both ends, it will act as a Frank-Read source when the load is applied. Cross slip events will generate dislocations on the 8 possible slip systems using the probabilistic law given in equation (2). The dislocation motion is restricted to the  $\gamma$ -matrix by the introduction of the impenetrable facets delimitating the  $\gamma$ - $\gamma'$  interfaces as depicted in Figure 5.

### 3. Results and discussion

#### 3.1 - Misfit stress calculations

The stress fields generated by the misfit are computed using a finite element analysis (Fig. 6). Assuming that the matrix and the precipitate both has a thermal expansion coefficient  $\alpha=10^{-5}$ , a temperature difference of 300 K is imposed between the  $\gamma$ -matrix and the  $\gamma'$ -precipitates. Then, the FE model finds the equilibrium state of the system assuming periodic boundary conditions along the (100) surfaces and a similar elastic modulus for both phases. The eigenstrain induced by the thermal expansion thus corresponds to a negative misfit  $\delta = -3.10^{-3}$  between the precipitate and the matrix.

Two of the stress field components are presented in Figure 6, namely  $\sigma_{11}$  and  $\sigma_{33}$ , since  $\sigma_{22}$  is identical to  $\sigma_{11}$  rotated  $90^\circ$ . In the matrix channel normal to [001] for instance, the two horizontal components  $\sigma_{11}$  and  $\sigma_{22}$  are maximum, compressive (blue color) and parallel to the  $\gamma$ - $\gamma'$  interface;  $\sigma_{33}$  the component normal to the interface is much smaller and tensile (red color). The shear stress component  $\sigma_{12}$  is given in Figure 6c. It is localized in the corner of the cuboid interfaces aligned with the Z-axis. Similar profiles are obtained by permutations for components  $\sigma_{13}$  and  $\sigma_{23}$ . The magnitude of the shear stresses in the horizontal and vertical channels is close to zero. Therefore, the stress field in the channels can be described as a quasi-planar compressive stress field with a peak in the center of the  $\gamma'$  face. By symmetry, the same is true in each of the three matrix channels.

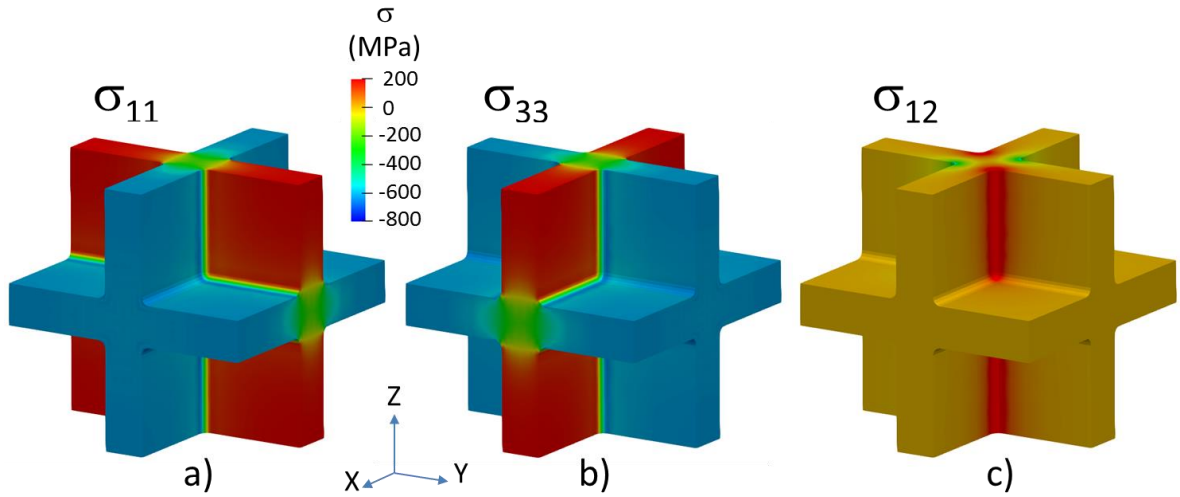


Fig. 6: Misfit stress components in the matrix channels, computed for  $\delta = -3.10^{-3}$ .

Eigenstrains induced by a negative misfit  $\delta = -3.10^{-3}$  between the precipitates and the matrix are described in Figure 7, namely  $\epsilon_{11}$  and  $\epsilon_{33}$ . It appears that a matrix channel is elongated in the direction normal to its bounding  $\gamma$ - $\gamma'$  interfaces, i.e. its width is increased by the misfit, with an amplitude maximal in the center of the faces of the  $\gamma'$  precipitates and minimal at the center of symmetry of the 8 cuboids considered in the simulation box (yellow-green colors at the crossing of channels).

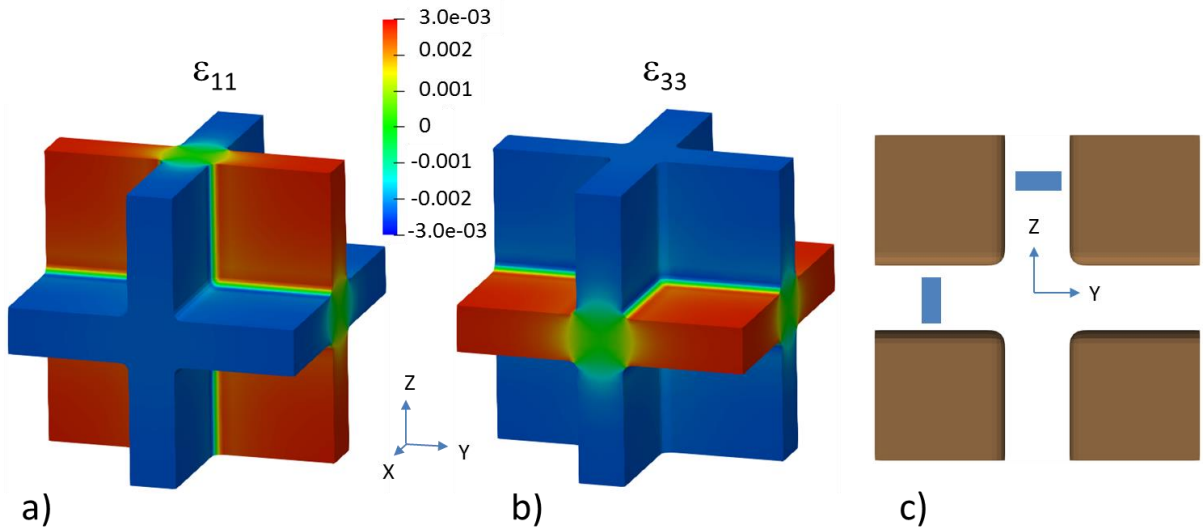


Fig. 7: Misfit strains in the matrix channels, computed for  $\delta = -3.10^{-3}$ .

Hence, the prestrain of each matrix channel resulting from the  $\gamma$ - $\gamma'$  misfit is simply a uniaxial elongation in the direction normal to the face of the cube as shown in the 2-D view (Fig. 7c).

### 3.2 - Activation of a slip system

A typical mapping of the shear stress resolved on the  $a/2(111)[-101]$  slip system (RSS) is given in Figure 8a, in the absence of any externally applied stress. One can see that the resolved shear stress varies between -495 and 495 MPa and that it is significantly different, on the average, in each channel. Therefore, we shall use thereafter the designation of channels for a given set of slip systems suggested by

Link et al., (2009). At the position of the dislocation sources, i.e. inside the horizontal channel, or propagating channel (P channel), this shear stress is  $\approx 280$  MPa. In the two vertical channels, the shear stresses are not equivalent. The vertical channel normal to the  $[010]$  direction, or repulsive channel (R channel) is loaded negatively, whereas the one normal to the  $[100]$  direction, or crossing channel (C channel), experiences hardly any resolved shear stress.

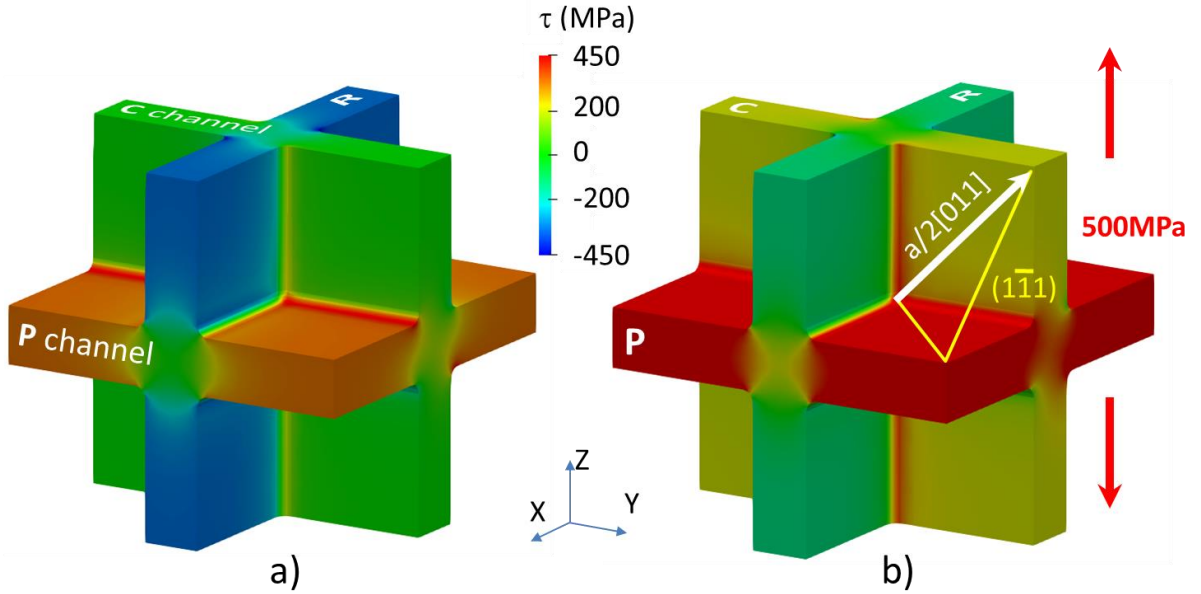


Fig. 8: Resolved shear stress induced on slip systems  $[011]$   $(1-11)$  or  $(11-1)$  and  $[0-11]$   $(111)$  or  $(-111)$ : a) by misfit alone. b) by misfit and tensile stress of 500 MPa along the vertical axis.

When a tensile stress of 500 MPa is imposed along the  $[001]$  direction, the RSS mapping is changed into the one plotted in Figure 8b. Because of crystal symmetries, 8 slip systems out of 12 can be activated simultaneously. These potentially active slip systems correspond to the 4 Burgers vectors introduced in Figure 5, each having two possible glide planes. They are forming two sets: those with Burgers vectors normal to the X direction, with RSS described in Figure 8 and those with Burgers vectors normal to the Y direction and having RSS rotated  $90^\circ$  around the Z direction with respect to the previous ones. Notice that the RSS in the horizontal channel is now higher than in the vertical channels. The RSS asymmetry between channels, induced by the misfit, is now amplified by the applied stress. Therefore, the main part of the plastic activity is expected to take place in the P channel, as repeatedly confirmed by numerous experimental observations (Link et al., 2009; Zhang et al., 2005; Pollock and Argon, 1994, 1992).

### 3.3 - Bowing out of the dislocations into the matrix channels: analytical estimate

Let us first examine the initial movement of perfect dislocations with Burgers vectors  $\mathbf{b} = a/2\langle 110 \rangle$  moving under a uniaxial stress applied along the Z axis. In this simplified analytical investigation, we will not consider the dislocation mutual interaction. They are bowing out from Frank-Read sources located in the center of the simulation cell (Fig. 4) and penetrating the various channels as they come in contact with the edges of the  $\gamma'$  cuboids. A first-order approximation consists in considering that the movement of the leading segments is controlled by a simple geometric rule relating to the width  $w$  of the channel, as for instance an Orowan stress. It yields a single value in the center of the 100 nm wide channels:

$$\tau_{\text{Or}} = A\mu \frac{b}{w} = A \times 80 \times 10^3 \frac{2.52 \times 10^{-10}}{100\sqrt{2} \times 10^{-9}} = A \times 140 \text{ MPa} \quad [3]$$

Where  $\mu=80$  GPa is the shear modulus of the  $\gamma$  matrix and  $A$  a coefficient close to 0.5.

The model presented here enables a more refined description of the local stress fields the dislocation is traveling through in channels clearly presenting drastic differences in resolved shear stress (Fig. 8). The force on a dislocation line of Burgers vector  $\mathbf{b}(b_1, b_2, b_3)$  resulting from the presence of these cumulated stress fields is given by the Peach-Koehler equation:

$$\vec{F}(\mathbf{U}) = \frac{a}{2} \begin{bmatrix} b_2 u_3 \sigma_{22} - b_3 u_2 (\sigma_{33} + \sigma_{appl}) \\ b_3 u_1 (\sigma_{33} + \sigma_{appl}) - b_1 u_3 \sigma_{11} \\ b_1 u_2 \sigma_{11} - b_2 u_1 \sigma_{22} \end{bmatrix} \quad [4]$$

where  $\mathbf{U}(u_1, u_2, u_3)$  is the local line vector of the dislocation,  $\underline{\sigma}$  is the local stress field combining the misfit stresses and  $\sigma_{appl}$  the external tensile stress applied along the Z direction. Notice that the Z component of this force is independent of  $\sigma_{appl}$ .

The glide force  $\vec{F}_U^{gl}$  on the segment of direction  $\mathbf{U}$  is the projection of  $\vec{F}(\mathbf{U})$  on the glide plane. Hence:

$$|\vec{F}_U^{gl}| = |\vec{F}| \sin \alpha = |\vec{F}| \sqrt{1 - \cos^2 \alpha} = \left[ |\vec{F}|^2 - (\vec{F} \cdot \vec{n})^2 \right]^{\frac{1}{2}} \quad [5]$$

where  $\alpha$  is the angle between the force on the dislocation and the normal  $\mathbf{n}$  to its glide plane.

And similarly; the force normal to the glide plane reads:

$$|\vec{F}_U^n| = |\vec{F}| \cos \alpha = \vec{F} \cdot \vec{n} \quad [6]$$

It is the climb force on an edge segment oriented along  $\mathbf{U}$ .

As an example, let us assume that the stress field in the channels of a [001] oriented single crystal under an applied tensile stress of 300 MPa along the [001] direction is constant and uniform. It is probably rather well verified in the central part of the channels. The computation was made for  $\mathbf{b}_2=a/2$  [011] gliding in plane (1-11). The forces were computed in each channel, respectively along two orthogonal directions: namely  $\mathbf{U}_{\parallel}$  (center columns Table II) characterizing the attraction or repulsion of the  $\gamma$ - $\gamma'$  interface for the dislocation line lying against it and  $\mathbf{U}_{\perp}$  (right hand columns Table II) giving an estimate of the driving force acting at the center of the bowing out segment of the dislocation. The resulting force reads:

$$\vec{F}(\mathbf{U}) = \frac{a}{2} \begin{bmatrix} u_3 \sigma_{22} - u_2 (\sigma_{33} + \sigma_{appl}) \\ u_1 (\sigma_{33} + \sigma_{appl}) \\ -u_1 \sigma_{22} \end{bmatrix} \quad [7]$$

The results presented in table II are illustrated by the schematic of Figure 9d where the glide forces are represented by red vectors with a surface area proportional to their magnitude. The climb forces are normal to the glide plane, hence to the plane of the figure.

- The glide forces are constant and uniform in the center part of each channel. Their amplitudes are equal on the screw segment and the bowing out arc, when it is assumed that the stress field is uniform in the channel, as is the case in this simplified model. They are exactly identical on the cross-slip plane (11-1) when the applied stress is exactly oriented in the [001] direction.
- It appears clearly that the largest glide forces are acting in channel P.
- In the C channel the glide force is 2.5 weaker than that in the P channel and the screw segments lying in the  $\gamma$ - $\gamma'$  interfaces are submitted to a rather strong force normal to the glide plane.
- In the R channel, under this applied stress of 300 MPa, the glide force is oriented in a way that would prevent the dislocation line from moving into the R channel, or pull it out if it had intruded that channel before, as shown in Figure 9d in E and F.
- In the P channel, the extra half plane associated with the edge component of the segment lying in the interface is pointing toward the inside of the  $\gamma'$  precipitates (in B, Fig. 9d).
- On the contrary, in the R channel, the extra half plane associated with the edge component is pointing away from the  $\gamma'$  precipitates and into the  $\gamma$  matrix (in E and F, Fig. 9d). It is due to the presence of a repelling force exerted by the  $\gamma$ - $\gamma'$  interface: it is made of a single component in the y direction (Eq [7]) and is equal to  $-\frac{a}{2}(\sigma_{33} + \sigma_{appl})$ ; it would only change sign and become attractive if the applied stress would overcome the local compressive component of the  $\gamma$ - $\gamma'$  misfit in the Z direction.

The actual change in penetration of the various channels depends so strongly on the stress level that a sequence of three steps computed by a DDD simulation is presented in figure 9 a, b, and c corresponding to the extension of a glissile  $a/2[011](1-11)$  loop under respectively 300, 400 and 600 MPa applied tensile stress. Notice that in these DD calculations, the internal stress field induced by all the dislocation segments is taken into account while this was neglected in the analytical estimates. Also the misfit stress used in the DD calculations is computed by FEM and includes all the components of the stress tensor (see Fig. 6).

- In Fig. 9, the “yield stress” of 300 MPa necessary to initiate plasticity in channel P (Fig. 9a), is raised up to 600 MPa (Fig. 9c) in order to show that closed loops in Superalloys with high  $\gamma'$  volume fractions are more likely to be diamond shape than triangle (as often sketched in the literature) since the third channel, the R channel, requires very high stresses to be penetrated by dislocations. Exceptionally, when the slip plane of a dislocation cuts the very apex of a  $\gamma'$  cuboid can a triangular loop form.
- In the P and C channels the climb forces, on the segment lying in the  $\gamma$ - $\gamma'$  interfaces (in B and D), are of opposite signs on the horizontal and vertical faces of the  $\gamma'$  cuboid, hence the first one is pointing into the  $\gamma'$  precipitate, thus pushing the dislocation into the precipitate, the latter one into the  $\gamma$  channel, thus pulling the dislocation away from the  $\gamma'$  precipitate. These screw dislocations, in channel C, connecting edge or near edge dislocations lying in the P channels were observed and well described by Zhang et al. (2005). They offer short distance

connections between adjacent faces of the  $\gamma'$  cuboids and modify, in opposite directions, the chemical potentials of  $\gamma$  and  $\gamma'$  atomic constituents on neighboring faces of the  $\gamma'$  cuboids. The chemical gradients between differently oriented faces, generated by the applied uniaxial stress, are thus enhanced and, by pipe diffusion, these arrays of interfacial connecting lines offer highly efficient diffusion routes to the migrating species. These chemical and diffusional processes are basic mechanisms in the implementation of the rafting of the  $\gamma$ - $\gamma'$  microstructure, as described by Carry and Strudel (1978) and observed by Schmidt and Fellerkniepmeier (1993). They were introduced in a DDD model simulating the octahedral glide and possible climb of dislocations during high temperature creep of a [001] oriented single crystal by Hafez Haghghat et al. (2013). But they remain beyond the scope of this paper that intends to deal with the micromechanical description, interpretation and numerical simulation of the elastoplastic interactions between precipitates and dislocations during the early stages of plastic deformation in nickel-based superalloys.

Misfit stress components (in MPa)	$\mathbf{U}_{\parallel}$ x $1/\sqrt{2}$	$\mathbf{F}_{\parallel}$ (MN/m) x $a/2\sqrt{2}$	$\ \bar{\mathbf{F}}_{\mathbf{U}}^{\text{gl}}\ $ glide	$\ \bar{\mathbf{F}}_{\mathbf{U}}^{\text{n}}\ $ normal	$\mathbf{U}_{\perp}$ x $1/\sqrt{6}$	$\mathbf{F}_{\perp}$ (MN/m) x $a/2\sqrt{6}$	$\ \bar{\mathbf{F}}_{\mathbf{U}}^{\text{gl}}\ $ Glide	$\ \bar{\mathbf{F}}_{\mathbf{U}}^{\text{n}}\ $ normal
Channel P $\begin{pmatrix} \sigma_{11} = -500 \\ \sigma_{22} = -500 \\ \sigma_{33} = 0 \end{pmatrix}$	$\begin{pmatrix} 1 \\ 1 \\ 0 \end{pmatrix}$	$\begin{pmatrix} -300 \\ 300 \\ 500 \end{pmatrix}$ in B	<b>23</b> in B	<b>-2</b> in B	$\begin{pmatrix} 1 \\ -1 \\ -2 \end{pmatrix}$	$\begin{pmatrix} 1300 \\ 300 \\ 500 \end{pmatrix}$ in A	<b>23</b> in A	<b>18</b> in A
Channel C $\begin{pmatrix} \sigma_{11} = 0 \\ \sigma_{22} = -500 \\ \sigma_{33} = -500 \end{pmatrix}$	$\begin{pmatrix} 0 \\ -1 \\ -1 \end{pmatrix}$	$\begin{pmatrix} 300 \\ 0 \\ 0 \end{pmatrix}$ in D	<b>9</b> in D	<b>6</b> in D	$\begin{pmatrix} 2 \\ 1 \\ -1 \end{pmatrix}$	$\begin{pmatrix} 700 \\ -400 \\ 1000 \end{pmatrix}$ in C	<b>9</b> in C	<b>25</b> in C
Channel R $\begin{pmatrix} \sigma_{11} = -500 \\ \sigma_{22} = 0 \\ \sigma_{33} = -500 \end{pmatrix}$	$\begin{pmatrix} -1 \\ 0 \\ 1 \end{pmatrix}$	$\begin{pmatrix} 0 \\ 200 \\ 0 \end{pmatrix}$ in F	<b>6</b> in F	<b>-4</b> in F	$\begin{pmatrix} 1 \\ 2 \\ 1 \end{pmatrix}$	$\begin{pmatrix} 400 \\ -200 \\ 0 \end{pmatrix}$ in E	<b>-6</b> in E	<b>-7</b> in E

Table II: Misfit stress components alone in the first column. Forces, under  $\sigma_{\text{appl}}=300$  MPa, on the dislocation segments lying in the  $\gamma$ - $\gamma'$  interfaces  $\mathbf{U}_{\parallel}$ , or bowing out into the channels  $\mathbf{U}_{\perp}$ .

Units of  $\|\bar{\mathbf{F}}_{\mathbf{U}}^{\text{xx}}\|$  are  $3.56 \cdot 10^{-3}$  N/m taking  $a=3.56$  Å. Locations A, B, ...F refer to Fig. 9d.

This example, which can be transposed, by rule of symmetry, to each of the three other potentially active slip systems, clearly shows that the spreading out of dislocations and their bowing out into the various matrix channels is not a simple geometric and 2-D Orowan problem, as suggested in the “first order approximation”. The internal stresses generated by the misfit between the two phases must be taken into account since they are similar in amplitude to the stresses applied during creep tests and definitely, during service.

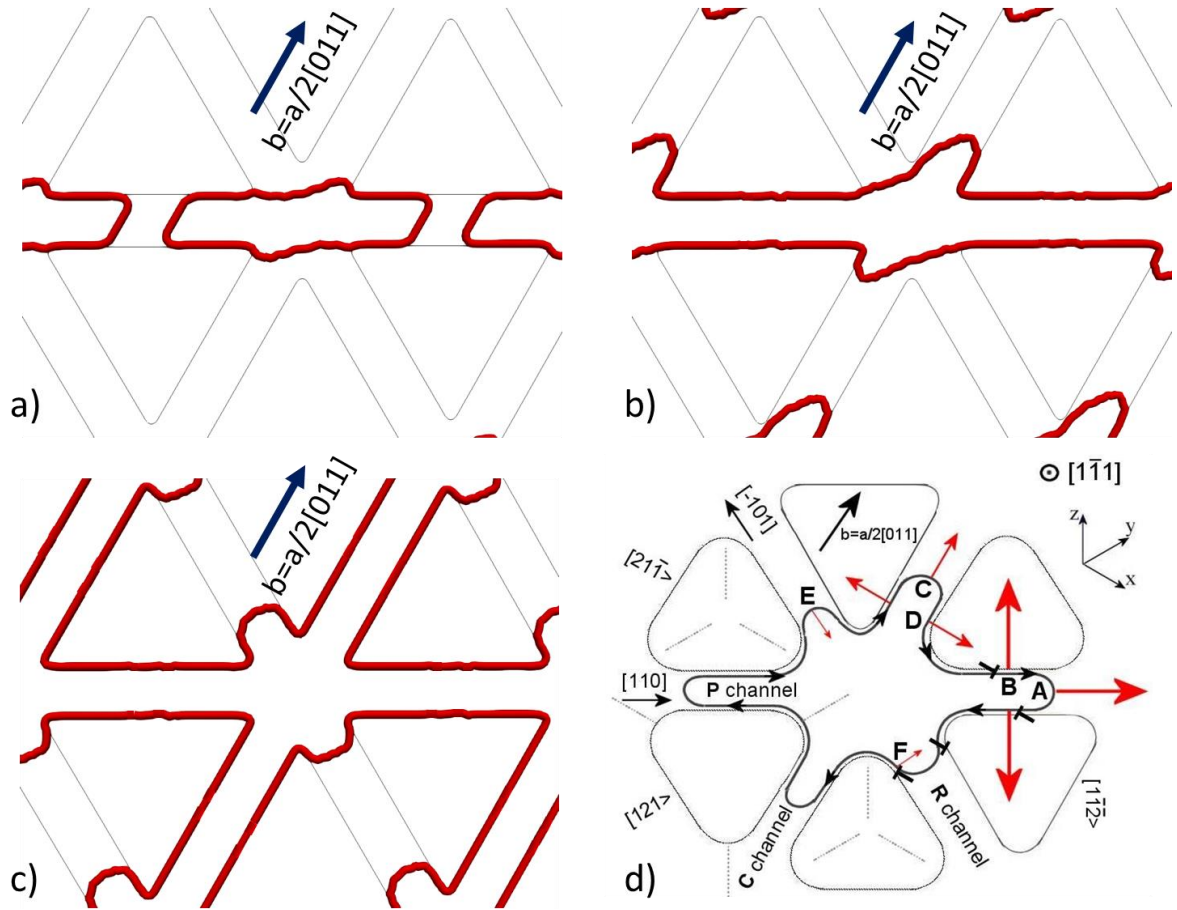


Fig. 9: Equilibrium dislocation configuration for a  $b=a/2[011]$  shear loop expanding in a (1-11) plane, within the misfit internal stress field and under different applied tensile stresses, before any cross slip event takes place. Snapshots of DDD simulations: a) under 300 MPa; b) under 400 MPa; c) under 600 MPa; d) Schematic with projected forces  $\mathbf{F}_{\parallel}$  and  $\mathbf{F}_{\perp}$  in red.

### 3.4 - Propagation, motion and multiplication of dislocations

Let us first consider a single slip system, namely  $a/2 [-101]$  matrix dislocations gliding either in the (111) or in the (1-11) planes and cross slipping freely as they move along the P channel. The elementary cell, where the computation is made, is duplicated along two directions in order to better illustrate the zigzagging progression of the slip system along the [010] direction (Fig.10). In the present model, these zigzagging segments of mixed  $60^\circ$  dislocations are unable to straighten out into pure edge dislocations along cube directions, since climb is ignored. This additional moving process is most important, especially at high temperature in connection with creep processes and was included in the improved version of this simulation scheme as proposed in Gao et al. 2017.

The tensile loading applied along the [001] direction is progressively increased from 500 MPa to 1000 MPa in a quasi-static manner: the stress is increased by 65 MPa after all dislocations have reached an equilibrium position. Figure 10 shows the dislocation microstructure reached after 4000 steps ( $\approx 0.3\%$  plastic strain). It confirms the adequate performance of the model since the dislocations are seen mainly traveling in the P channel and can also penetrate fairly easily the C channel, the more so the applied stress is increased, but they remain impeded from penetrating the R channel, as they are seen waiting and accumulating at its

entrance. Frequent cross slip events in the P channel are well illustrated by Figure 10b where the dislocations are imaged with the Burgers vector end on.

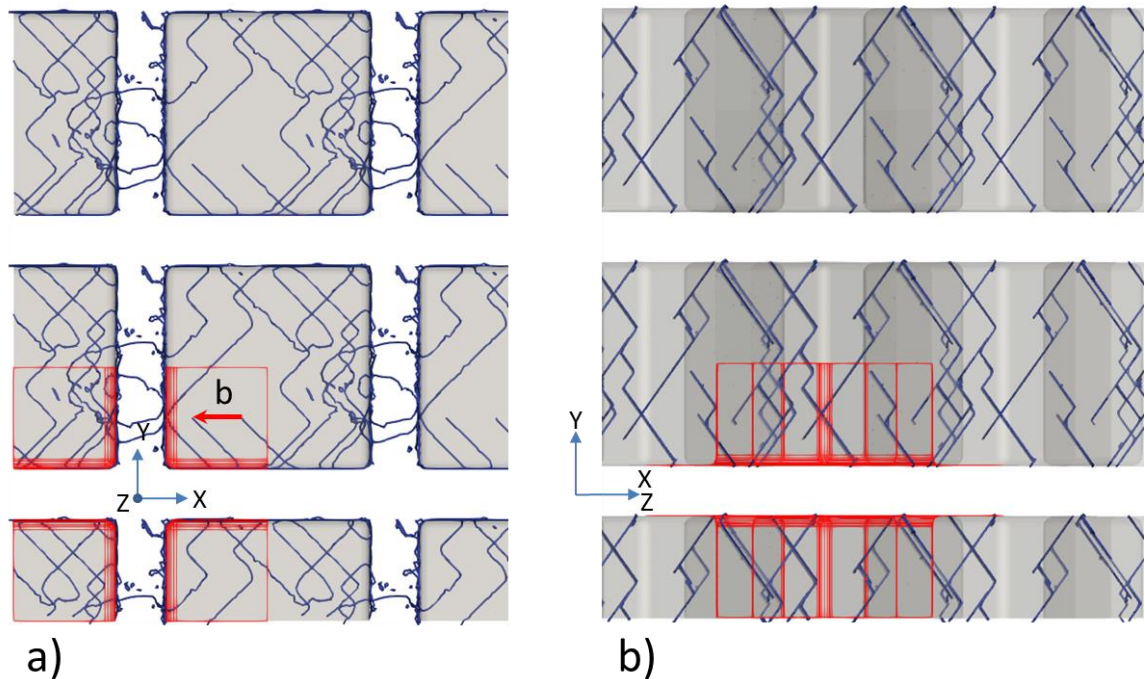


Fig. 10: Cross slip scene. The elementary computation box is drawn in red in the lower left hand corner. a) View along  $[001]$ ; b) View along  $[-101]$ .

If we now examine the simultaneous operation of two sources of dislocations namely  $a/2 [-101]$  (in blue, Fig. 11) and  $a/2 [011]$  (in red, Fig. 11) sharing a common slip plane (1-11), we see that the distribution of dislocations, observed along the loading direction  $Oz$ , is quite uniform.

The probability for cross slip is an adjustable parameter in this model. In Figure 11b, the cross-slip ability was arbitrarily enhanced, so that many dislocation lines are now oriented along the  $(100)$  and  $(010)$  directions. Experimental observations by TEM (Fig. 3a, Pollock and Argon, 1992, Zhang et al., 2010; Pollock and Field, 2002) clearly indicate that the spacial frequency of cross slip is  $\approx 200$  nm, hence once or twice across a  $\gamma-\gamma'$  interface and once more at the crossing of the C channel as explained by Link et al. (2009). Whatever the detailed mechanisms of restoration are (climb, pipe diffusion of vacancies and various atomic species,...), the zigzagging dislocations will shorten their length by straightening out into  $\langle 100 \rangle$  directions. Notice that this dislocation motion will take time since diffusion is two order of magnitude slower than glide. Yet it seems to be implemented within a couple microns behind the cross slipping and leading screw segment during creep at  $850^\circ\text{C}/190$  MPa, as evidenced in C and on the left of point A on Fig. 3b. Hence the cross slip ability retained for the model was adjusted here to fit the experimental observations as can be seen on fig. 10 and fig. 11a.

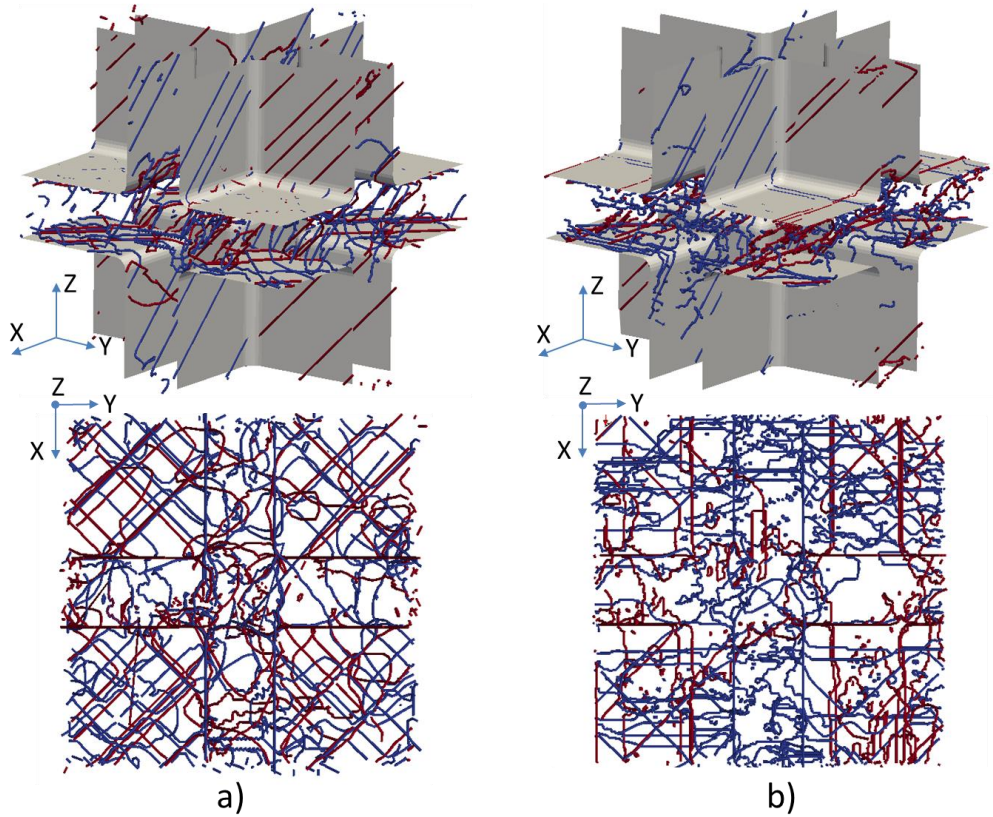


Figure 11: Dislocation microstructure formed from two screw dislocation sources  $a/2$   $[-101]$  (in blue) and  $a/2$   $[011]$  (in red) when (a) cross-slip is limited or (b) enhanced.

On the other hand, in the vertical channels, whatever the cross slip probability, the line orientations lie along the  $[101]$  and  $[011]$  directions. Hence, we can conclude that cross-slip has no effect on the dislocation patterning in the vertical channels, whereas it plays a major role in the movement and patterning of dislocations in the horizontal channel.

### 3.5 Mechanical response

During the first stages of plasticity, dislocations are emitted from sources located mainly in subboundaries in single crystals and in grain boundaries, twin boundaries and carbides in polycrystals. In nickel base superalloys, because of the large volume fraction of  $\gamma'$  precipitates, they immediately and almost exclusively interact with them and their stress fields rather than with each other. In so doing, they introduce their own stress field and deeply modify the pre-existing internal stress fields. The present model, by combining DDD and FEM can adequately image the strongly heterogeneous stress fields resulting from these interactions. This ability is illustrated in the following micrographs taken from the previous example where two interacting sources are operating and the simulation was interrupted after 1868 steps, when the applied stress reached 875 MPa.

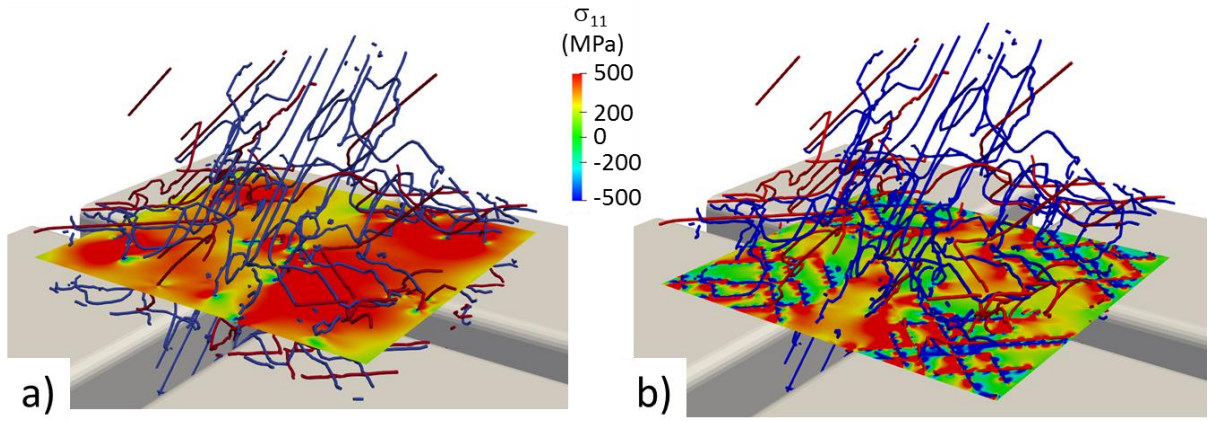


Fig. 12: Stress component  $\sigma_{11}$  resulting from the presence of dislocations alone, after applying 875MPa in 1868 steps. a) at mid P channel and b) at  $0.05w$ .

We see that the density of dislocations in the P channel is such that their presence has more than compensated the compressive biaxial stress field produced by the  $\gamma$ - $\gamma'$  misfit since a situation of biaxial tension (red color dominating) is now pervading in the central part of the channel (Fig.12a). Near the  $\gamma$ - $\gamma'$  interfaces of the P channel (Fig.12b) the resulting stress field is less uniform than in the center of the channel, due to the vicinity of the dislocation lines, but it is well compensating the  $\gamma$ - $\gamma'$  misfit, on the average, near the interfaces (gray color) and definitely tensile in the crossing of the vertical channels C and R, away from any immediate interface.

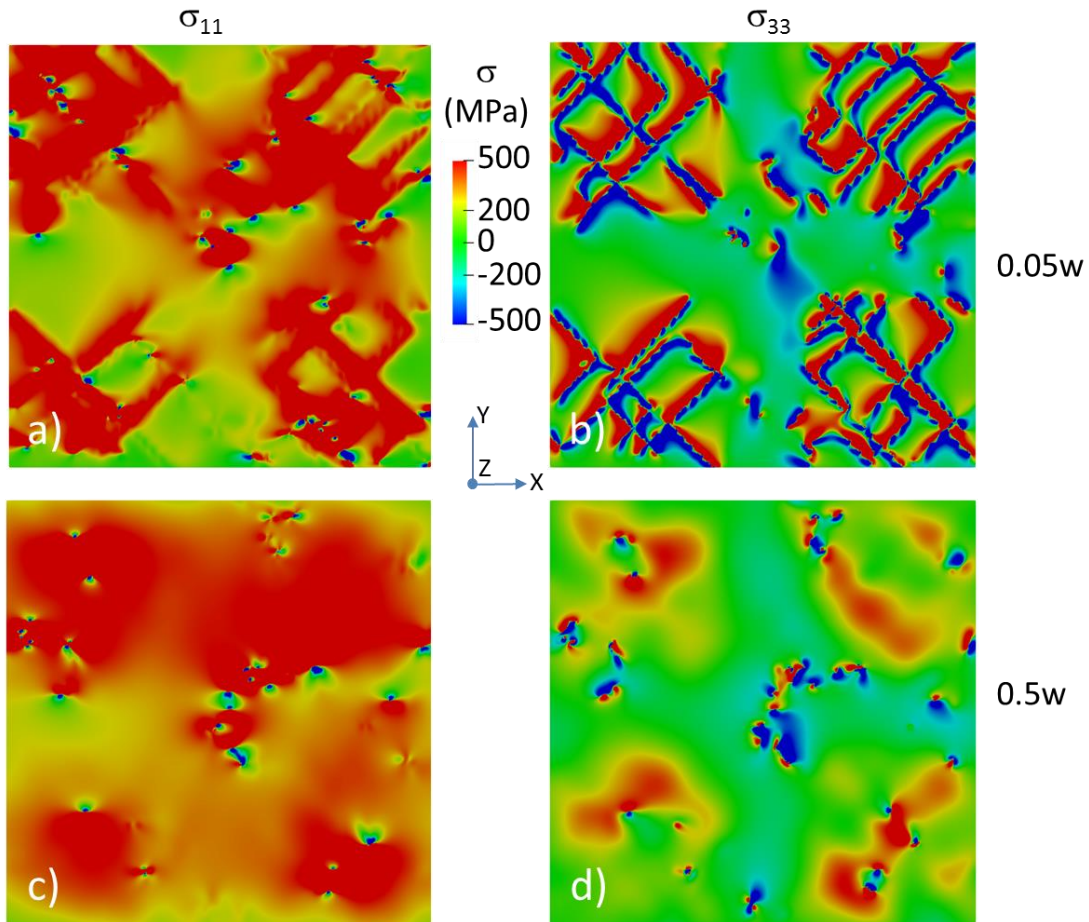


Fig. 13: Stress components resulting from the presence of dislocations alone after applying  $\sigma_{\text{app}}=875\text{MPa}$  in 1868 steps a)  $\sigma_{11}$ ; b)  $\sigma_{33}$  at  $0.05w$  and c)  $\sigma_{11}$ ; d)  $\sigma_{33}$  at  $0.5 w$ , mid P channel.

If we now compare the biaxial stress field ( $\sigma_{11}, \sigma_{22}$ ) and the uniaxial vertical stress field  $\sigma_{33}$  in the middle of the P channel mapped across the elementary cell of the model (Fig. 13), we see that, at this point of the plastic deformation, the  $\gamma$ - $\gamma'$  misfit is fairly well compensated in that channel at the verge of the  $\gamma'$  precipitates (Fig. 13a and 13c) but that the applied stress (along Oz) is still weaker than the Z component of the misfit stresses within the vertical channels (compressive, blue regions in Fig. 13b and 13d). At higher applied stress (1200 MPa) and larger plastic strain, the same situation prevails, despite the higher density of dislocations (Fig. 14a and 14b) since their presence in the vertical channels is aggravating the misfit rather than compensating it (Fig. 9d). Pushing this model which assumes non-shearable particles having a strong misfit stress field to its upper limits, we show that the development of the dislocation microstructure, even after large cumulated plastic strain, is still governed not only by the applied stress but still very much by the local stress field that it tends to compensate.

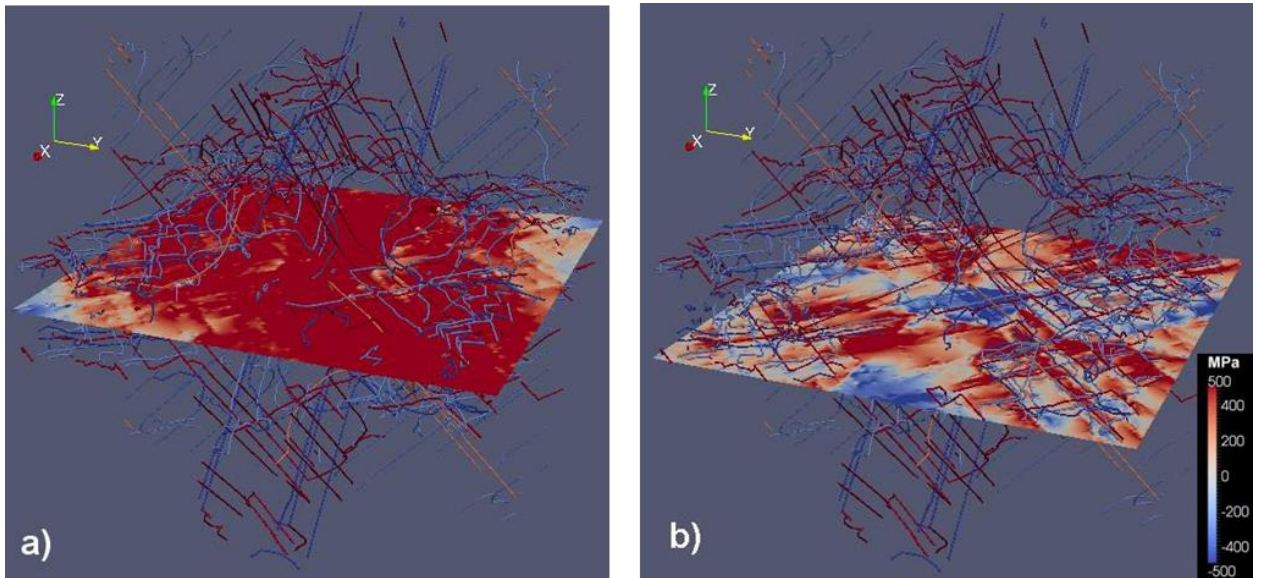


Fig. 14: Stress components resulting from the presence of dislocations alone after applying  $\sigma_{\text{app}}=1200\text{MPa}$ . a)  $\sigma_{11}$  or  $\sigma_{22}$ , at mid P channel and b)  $\sigma_{33}$  at mid P channel.

Let us consider now the strain fields: initially, the matrix channels are prestrained elastically in elongation along Oz by the  $\gamma$ - $\gamma'$  misfit stress fields, in the direction normal to the  $\gamma$ - $\gamma'$  interfaces. All channels are elastically thickened by this internal stress field distribution. According to Hooke's law, the plane stress exerted by the misfit across the horizontal channel, for instance reads:

$$\epsilon_{33}^{\text{misfit}} = -\frac{\nu}{E}(\sigma_{11} + \sigma_{22}) = -2\nu\delta > 0 \quad [8]$$

since  $\sigma_{11} = \sigma_{22} = E\delta$  in that channel. Note that all misfit quantities are negative,

The introduction of an applied uniaxial stress  $\sigma_{\text{appl}}$  will break the initial symmetry between channels and initiate plasticity by introducing dislocations and their associated additional stress field. In particular, let us examine the horizontal channel, which is most exposed to their activity (forward plastic flow induced by  $\sigma_{\text{appl}}$ ) and to their presence in the  $\gamma$ - $\gamma'$  interfaces where they relax most of the misfit stresses.

Figure 15 shows the various contributions to the  $\varepsilon_{zz}$  component of the strain during the simulation. The plastic strain is computed from the area swept by the dislocation lines during tensile straining. This component increases during the simulation up to a cumulated plastic strain of  $\varepsilon_{zz}^p = 0.7 \times 10^{-4}$  (DDD plastic, pink curve, Fig. 15). Meanwhile the local arrangement of dislocations induces an elastic relaxation of the pre-thickened horizontal channel. This recovered elastic strain (DDD elastic, red curve figure 15) reaches  $\varepsilon_{zz}^e = -1.8 \times 10^{-4}$  at the end of the simulation sequence.

Summing up the two contributions, we finally obtain an overall contraction of the channel of  $1.1 \times 10^{-4}$  along the tensile direction. The light blue line (Fig. 15) is the elastic strain of the material under 1200 MPa before any plasticity occurred and the dark blue curve the resulting contraction of the material (total strain i.e., elastic + plastic) as plasticity develops and added interfacial dislocations progressively cancel out the misfit stress fields within the P channel. Notice that only a few dislocations have moved after 500 steps, hence the small amplitude of all strains.

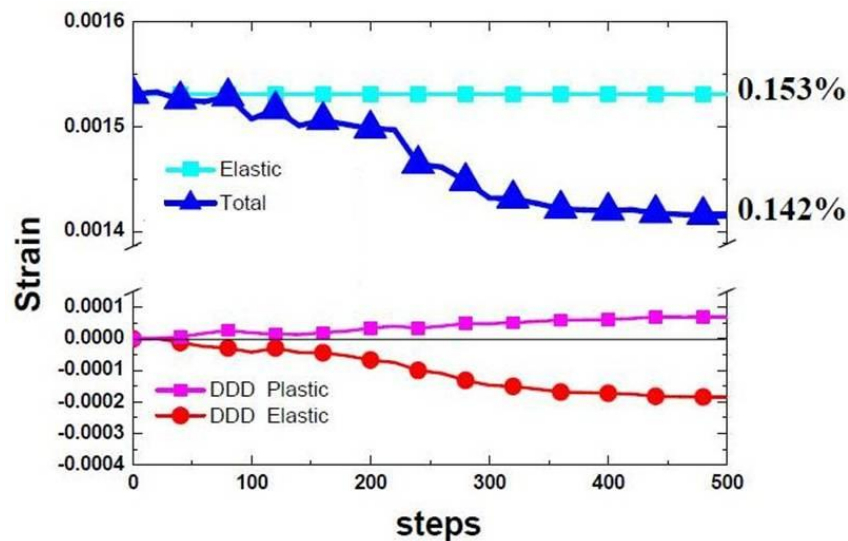


Fig. 15: Evolution of  $\varepsilon_{zz}$  strain components in the horizontal channel, during the first stages of plasticity under uniaxial loading along Oz.

Experimentally, this unusual behavior has been described as “negative creep” in superalloys. It was first reported in the 80’s by Reppich (1984) who could set it aside from the volume contraction taking place in these alloys when a residual precipitation of the  $\gamma'$  phase occurs at the test temperature. This apparently paradoxical contraction under tensile stress was correctly interpreted by Louchet (1995) as a process of minimization of the free energy of the material when placed under a tensile stress (Ratel et al., 2009) but was improperly attributed to the rafting of the microstructure, when it is simply concomitant. As creep progresses, the movement of perfect matrix dislocations is made easier by the widening of the P matrix channels

resulting from the rafting and the coarsening of the microstructure. These processes are stimulated by the internal stress field distribution generated by the  $\gamma$ - $\gamma'$  misfit and diffusion is

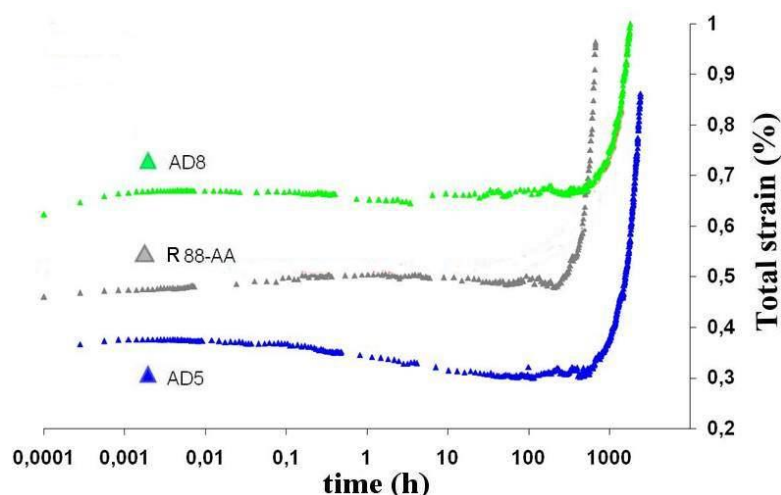


Fig.16: Total strain (elastic + plastic) during creep of three PM disc alloys at 700°C under 650 MPa. Notice the long “incubation period” of alloys AD8 and René 88 and the negative creep rate of the most resistant alloy AD5 (Augustins-Lecallier, 2012)

enhanced in the core of dislocations. In nickel base superalloys, this rafting phenomenon is necessarily preceded by the micro-mechanisms described in this model. It is actually biased by the applied stress field Pineau (1976) but also requires diffusional processes, abundantly activated during creep at high temperature and enhanced by the presence of interfacial dislocation networks (Carry and Strudel, 1978; Strudel, 2007).

The experimental recording of negative creep is rather difficult since it requires a fully stabilized material (absence of residual  $\gamma'$  precipitation), a high thermal stability of the extensometer and a low noise (better than  $10^{-9}s^{-1}$ , on the strain rate). In order to avoid the triggering of additional mechanisms of plasticity taking place during later stages of creep or under high stress levels, very low stresses must be applied for fairly long times ( $> 1000$  h). In the development program of PM alloy N 19, three different alloy compositions, with  $\gamma'$  volume fractions higher than 40%, were tested in creep at 700° C under the same stress of 650 MPa. The creep curves are presented in Figure 16 where a (log t) scale is used in order to stretch out the primary stage of creep. For the two lesser resistant alloys (AD-8 and René 88) their creep rate remains quasi-null for several hundred hours, thus indicating that shrinkage due to elastic relaxation along the Z direction is just about compensated by the forward elongation associated with the plasticity of this initial stage II. On the other hand, the more resistant alloy AD-5 clearly exhibits negative creep under the selected stress of 650 MPa.

These results together with the neutron diffraction *in situ* measurements of lattice parameters (under applied stress and after straining of PM alloy RR 1000, Lu et al., 2008) clearly imply that, regardless of grain orientation the first active populations of dislocations are mobilized to cancel out some of the numerous pre-existing internal elastic strain fields generated within the crystals by the misfit of  $\gamma'$  precipitates of all sizes.

### 3.6 Ideal interfacial networks

In the absence of any externally applied stress, when  $\gamma'$  precipitates are in the micron range and above, matrix dislocations, stored in the subgrain boundaries, move spontaneously at

high temperature, during aging at 1000°C/24h in AM1 alloy for instance (Fredholm et al., 1988; Long et al., 2016) and cover the overgrown precipitates with 3-D edge oriented networks of edge dislocations (Lasalmonie and Strudel, 1975). Under these conditions, the mesh size  $d$  of the equilibrium edge networks that best compensate for the existing misfit, is given by Brooks formula (Brooks, 1952):

$$d = \frac{b}{|\delta|} \quad [9]$$

where  $b$  is the modulus of the projection of the Burgers vector of the dislocations onto the  $\gamma$ - $\gamma'$  interface and  $\delta$  the misfit parameter. For a nickel base superalloy with lattice parameter  $a=3.56$  Å, then  $b=a/2$  and with a misfit parameter  $|\delta| = 3.10^{-3}$ , the equidistance of dislocation lines is 60 nm.

During creep at intermediate and high temperatures (650°C to 1100°C) and under a low enough applied stress where the matrix is plastically deformed but the  $\gamma'$  precipitate are not sheared, matrix dislocations with  $\underline{b}=a/2 \langle 110 \rangle$  can move into the matrix channel normal to the applied tensile stress, the P channel (as described in § 3.4), under the combination of the applied stress and the local stress fields generated by the  $\gamma$ - $\gamma'$  misfit. They are generally observed to progress into the channels by repeated cross slip on  $\langle 111 \rangle$  planes and their initial zigzag aspect results from their immobilization in the directions common to their slip planes and the  $\gamma$ - $\gamma'$  interfaces. By climb in these interfaces, they rapidly shorten their length by straightening out from their  $\pm 60^\circ$  orientations into pure edge, cube orientations; a configuration that best compensates the pre-existing stress fields [Carry and Strudel, 1975; Lasalmonie et Strudel, 1975]. They have been observed covering hundreds of rafted  $\gamma'$  precipitates after longtime creep under low stress by Zhang et al. (2005).

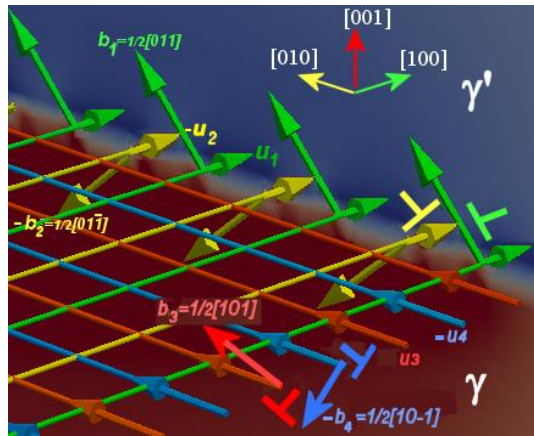


Fig. 17: Details of Burgers vectors  $\underline{b}_i$ , line vectors  $\underline{u}_i$  and extra half plane orientations used in the description of an ideal  $\gamma$ - $\gamma'$  interfacial dislocation network.

Under a uniaxial stress applied along the Z axis, four different Burgers vectors can be activated. Considering that each of them is associated with an array of parallel edge dislocations, periodically spaced by 60 nm, with cube orientations [100] and [010] in the horizontal plane ( $\underline{U}_i$  vectors), we end up with a square grid of dislocation lines (Fig. 17), each, lying in the  $\gamma$ - $\gamma'$  interface, with their extra half plane pointing toward the precipitate. This idealized dislocation network is generating, in the P channel, a dipolar stress field of significant intensity. Its computed components are represented on Figure 18. Notice that:

- they are generally similar to the components of the stress fields generated by the  $\gamma$ - $\gamma'$  misfit but of opposite sign (Ratel et al., 2010).
- the vertical component of the stress field  $\sigma_{33}$  (Fig.18b) is almost null in the channel, except in the immediate vicinity of the dislocations where it is strongly nonuniform.
- on the other hand, the planar biaxial stress field ( $\sigma_{11}$ ,  $\sigma_{22}$ ) is quite uniform and strong across the P channel (Fig.18a), exhibiting minor variations in the vicinity of the lines, as expected.
- the width of the channels (100 nm) being close to the distance between interfacial dislocation lines (80 nm), the stress fields generated by this array of dislocations is hardly perturbed by the crossing of the vertical channels.

If we assume that the stress fields are completely uniform in the P channel, a simple estimate of the elastic and plastic components of the strain associated with the development of such ideal dislocation networks can be made. The elastic relaxation of the pre-widened channel P is given by the equation [8] and yields:

$$\varepsilon_{33}^{relax} = -2\nu\delta = 2 \times 0.33 \times 3.10^{-3} \approx 2.10^{-3} \quad [10]$$

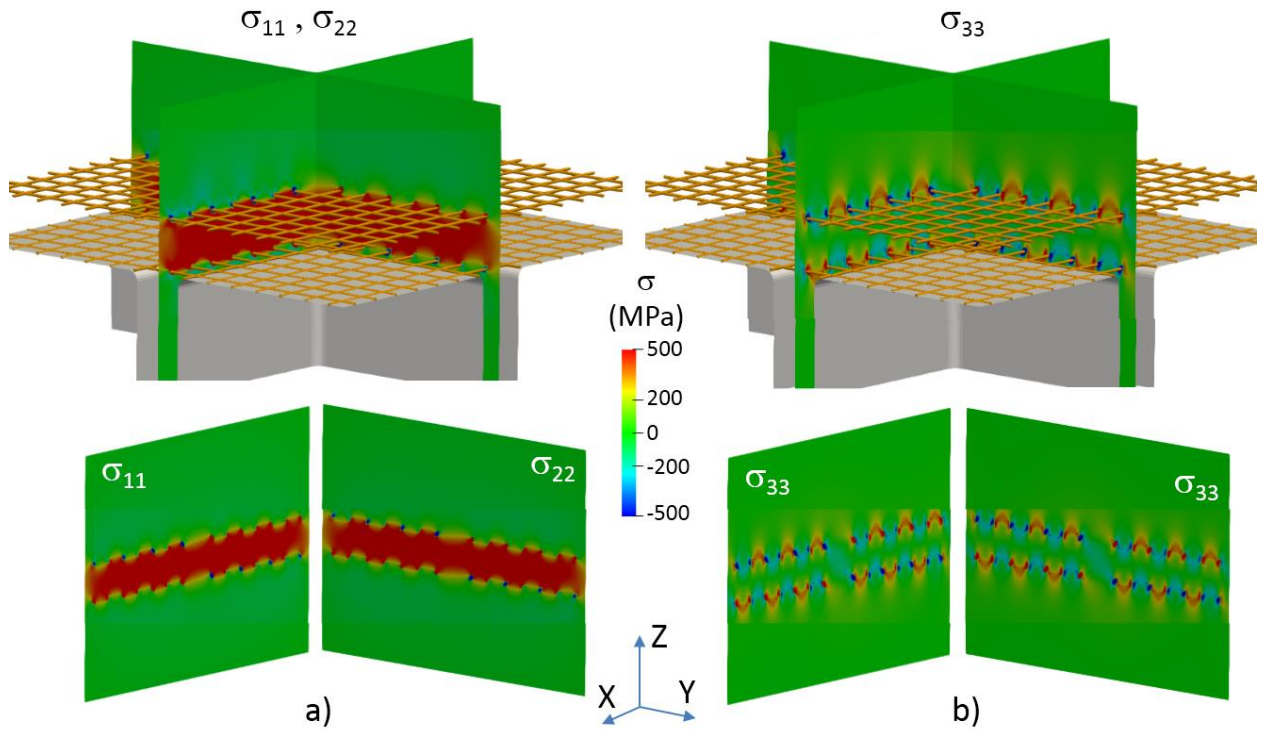


Fig.18: Ideal interfacial dislocation network in channel P in absence of misfit stress fields and associated internal stress field a)  $\sigma_{11}$  or  $\sigma_{22}$  ; and b)  $\sigma_{33}$ .

On the other hand, the plastic strain generated by the movement and multiplication of dislocations crisscrossing across the P channel in order to generate this ideal array, can be

calculated by estimating the total area swept:

$$\varepsilon_{33}^{plastic} = b\rho L = \frac{a}{2}\rho\frac{w}{2} = 1.8 \times 10^{-10} \times 10^{14} \times \frac{10^{-7}}{2} = 0.9 \times 10^{-3} \quad [11]$$

since  $\rho$ , the dislocation density in the elementary simulation cube (size  $L^3$ ) is the sum of twice (2 orthogonal directions in the horizontal plane) 4 pairs of dislocations (with  $b=[\pm 101]$ ) with 60 nm distance between lines, in each interface of the channel ( $\times 2$ ), hence:

$$\rho = \frac{16 \times 2 \times L}{L^3} = 32L^{-2} = 32 \times (0.5 \times 10^{-6})^{-2} = 1.28 \times 10^{14} \quad [12]$$

This simple calculus clearly confirms the result of the simulation presented in Figure 16 showing that the elastic relaxation of the pre-widened P channel, provided by the development of interfacial dislocation networks, is significantly larger than the plastic strain produced by the movement of dislocations during the first stages of plasticity, in nickel base superalloys at high temperature. However, this simple calculus yields an upper bound to the amplitude of the contraction taking place during the first stage of creep, since it is assuming that this elastic relaxation is taking place uniformly throughout the test sample and is also the sole mechanism of plasticity taking place during that stage. In reality, plasticity is nonuniform throughout the gauge length under control, some areas may still be undeformed when others are already involved in more advanced stages of creep with higher rates of plasticity which involve shearing of precipitates, migration of grain boundaries, climb, recombinations, annihilations and other restoration processes.

Finally we investigate the elastic stress field that would induce a perfect periodic square grid of  $a/2[\pm 101]$  and  $a/2[0\pm 11]$  edge dislocations, similar to the previously described network but located away from each other by 500 nm and centered in the middle of a large  $\gamma'$  precipitate (Fig. 19). Most of the general features are similar to the previously described dipolar wall, except for the uniform aspect of the fields which now spread out without much decay between the two polar walls of opposite signs.

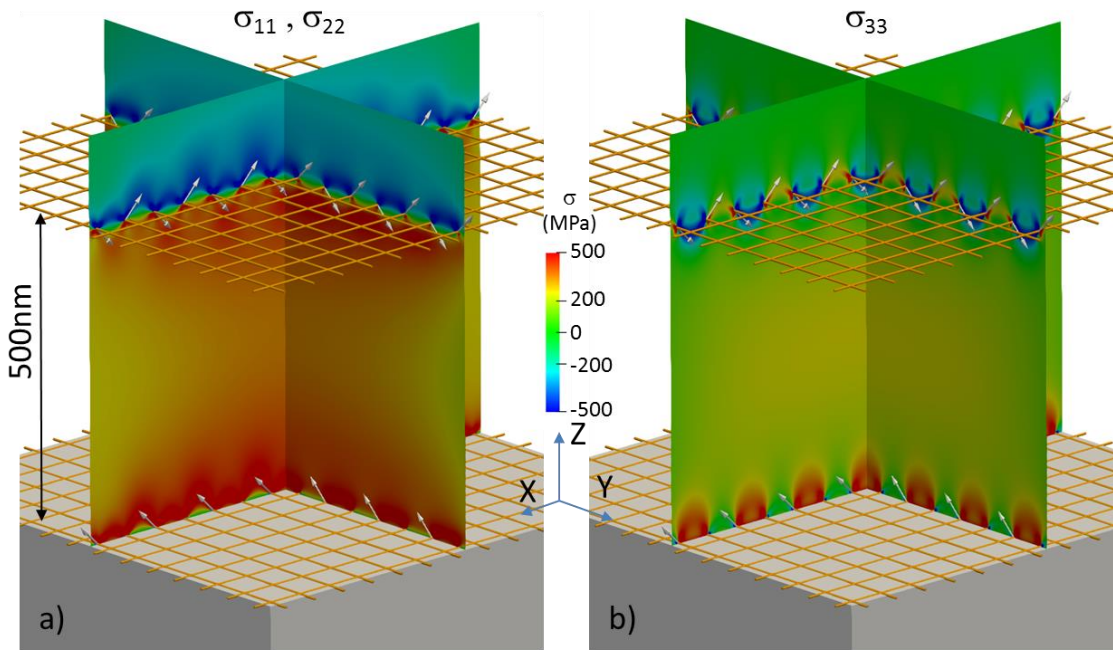


Fig. 19: Ideal  $\gamma$ - $\gamma'$  interfacial dislocation network at large distances ( $w=500$  nm) and associated stress field components a)  $\sigma_{11}$  or  $\sigma_{22}$  and b)  $\sigma_{33}$ . Arrows corresponds to the Burgers vectors of each dislocation line.

In polycrystalline materials used for discs, the volume fraction of  $\gamma'$  precipitates is over 40% and large precipitates (in the micron range or over) are scattered throughout individual grains where finer secondary and tertiary precipitates are also present. Although these larger precipitates are no longer closely aligned in quasi-periodic manner as in single crystals, the situation we have concentrated most of the simulation so far, nevertheless we can see that similar stress fields can develop and produce similar relaxation effects during the first stages of plasticity in polycrystalline materials. This point is confirmed experimentally, in Fig. 16 where the creep curves of polycrystalline alloys under 650 MPa tensile stress at 700°C, exhibit either a prolonged period of several hundred hours without any detectable strain or even a contraction ranging to about  $10^{-3}$ , before it starts flowing forward in the tensile direction; a behavior often and improperly described in the literature as “incubation period”.

When building these idealized networks, it was assumed that the dislocations would cross each other at right angle without interacting. In reality, they do recombine and form square arrangements of lines [Pollock and Field, 2002; Lasalmonie and Strudel, 1975] with Burgers vectors  $a/2[\pm 110]$  and  $a/2[1\pm 10]$ . Notice that these dislocations exhibit an extra half plane not only pointing toward the  $\gamma'$  precipitate but directly perpendicular to the interface, thus directly contributing to the compensation of misfit. On the other hand, they should remain inactive since their Burgers vectors are normal to the applied stress.

## CONCLUSION

In nickel base superalloys primary creep is very important since it covers most of the service life of critical engineering parts such as discs or blades. Therefore, developing a reliable model describing, in details, the first stages of plasticity taking place in a wide range of temperatures (500°C to 1100°C) offers the tool for an appropriate and quantitative interpretation of the unusual minimum creep rate exhibited by these  $\gamma'$  strengthened alloys.

The micromechanical model presented here is a combination of FEM, which provides updated detailed mapping of local stress fields and DDD techniques which describe the multiplication and movement of perfect dislocations within the prestrained channels of the  $\gamma$  matrix. For the sake of simplicity, it is based on a strictly triperiodic arrangement of identical  $\gamma'$  cuboids having a misfit parameter  $\delta = -3.10^{-3}$  with the matrix.

This model confirms that the negative  $\gamma$ - $\gamma'$  misfit induces an in-plane equi-biaxial stress in each channel parallel to the interface that results, in the orthogonal direction, in an elastic elongation of the width of the channel:

$$\varepsilon_{33}^{misfit} = -\frac{\nu}{E}(\sigma_{11} + \sigma_{22}) = -2\nu\delta > 0 \text{ for instance.}$$

When a tensile load is imposed along the (001) axis, an asymmetry is introduced which biases the first stages of plasticity. Slip systems, involving dislocations with four different Burgers vectors are equally activated, each with equal probability of cross slip on two different

planes. The channel normal to the tensile stress (channel P) is penetrated under local stresses lower than the Orowan stress, since it is attractive for these dislocations. The channel parallel to the tensile stress and the Burgers vector (channel C), where the dislocations leave the screw dipoles in the  $\gamma$ - $\gamma'$  interface is explored next. The other vertical channel (channel R), where the edge component of the dislocations would aggravate the misfit rather than compensate for it, is repulsive to the dislocations and would only be penetrated under high applied stress.

Thus, a specific arrangement of near edge dislocations develops at the  $\gamma$ - $\gamma'$  interface of the P channel which progressively relaxes the elastic pre-strain prevailing initially in this channel. In reality, it is observed that climb in these interfaces enables zigzagging segments of  $60^\circ$  dislocations to straighten out into pure edge perfect dislocations, oriented along the cube directions, with their extra half plane's pointing into the  $\gamma'$  precipitates and thus efficiently compensating the misfit in channel P. The proposed model, in its present form, cannot describe this particular stage of primary creep since it does not include any diffusional mechanism.

It is shown that the development of this square grid of dislocations in the P channel produces an elastic relaxation along the tensile axis, the amplitude of which is larger than the forward plastic strain in that direction, assuming that this mechanism is acting alone and uniformly across the creeping part or test piece. These latter conditions are rarely met in practice, but when they are, under carefully applied low stresses for instance, these findings explain the negative creep results observed experimentally during the initial stage in Ni based superalloys, single crystals and polycrystals as well.

The bipolar stress field generated by an idealized square network of straight and pure edge dislocations of opposite signs lying in two parallel planes was computed in order to compare it with the stress field generated by the  $\gamma$ - $\gamma'$  misfit in the matrix channel, assuming similar elastic moduli of both phases. Making use of Brook's formula, the distance between dislocations was chosen to exactly compensate for the selected misfit of  $-3.10^{-3}$ . As expected, the field is rather heterogeneous at distances from the dislocations equivalent to their equidistance, but rapidly becomes uniform, with a predominant plane stress tensile nature, exactly opposite to the plane stress compressive nature prevailing in the matrix channels. This clearly indicates that the quasiperiodic dislocation networks observed after creep in the  $\gamma$ - $\gamma'$  interfaces are effectively compensating for the misfit and that their interconnections between P channels, promoting paths for pipe diffusion become main channels for microstructural rearrangements taking place during creep and called rafting. The micro-mechanisms described in the present model are the forerunners of this phenomenon, widely observed during creep in nickel base superalloys.

### **Acknowledgements**

This research was carried out under Project ANR-07-MAPR- 0023-04 CAT-SIZE Matériaux et Procédés which provided the financial support for Dr H.J. Chang. We also acknowledge the financial support of DGA, through the PROMETHEE program, that offered a framework for the alloy development program N-19 launched and guided by SAFRAN Motors. The authors also gratefully acknowledge the fruitful and stimulating discussions and the enthusiastic support of S. Forest.

## References

- Augustins-Lecallier I., 2012. Design of new PM nickel base superalloys for turbine discs. Thesis in French. Mines-ParisTech. Centre des Matériaux, BP-87, 91003-EVRY-Cedex (France).
- Bonneville J., Escaig B., Martin J.L., 2002. A study of cross-slipping activation parameters in pure copper, *Acta Metall.* **36**, 1989–2002.
- Brooks, 1952. Theory of internal boundaries, In *Metal Interfaces*, Am. Soc. Metals, Cleveland, Ohio, 20-65.
- Carry C. and Strudel J.L., 1975. Direct observation of  $\langle 110 \rangle$ - $\{1-10\}$  in FCC single crystals of a Ni base superalloy. *Scripta Met.* **9**, 731.
- Carry C. and Strudel J.L., 1978. Apparent and effective Creep Parameters in Single Crystals of a Nickel Base Superalloy, Part II: Secondary Creep. *Acta Metall.* **26**, 859-870.
- CAST3M, Finite element software developed by CEA and available at [www-cast3m.cea.fr](http://www-cast3m.cea.fr)
- Devincre B., Kubin L.P, Lemarchand C. and Madec R., 2001. Mesoscopic simulations of plastic deformation. *Mater. Sci. Eng.* **A309-310**; 211-219.
- Dirand L., Cormier J., Jacques A., Chateau-Cornu J.P., Schenk T., Ferry O. and Bastie P., 2013. Measurement of the effective  $\gamma$ - $\gamma'$  lattice mismatch during high temperature creep of a Ni-based single crystal superalloy. *Materials Characterization* **77**, 32-46.
- El-Haziz M.E., 1986. Correlation between tensile and creep data in Alloy 800H at 850°C. *J. Nucl. Mat.* **231**,146-150.
- Epishin A. and Link T., 2004. a) Mechanisms of high temperature creep of nickel based superalloys under low stress. *Phil. Mag.*84, 1979-2000. b) Mechanisms of high temperature creep of nickel based superalloys under low applied stress. *Superalloys 2004*. Publisher TMS, the MMM Society, 137-143.
- Fredholm A. and Strudel J.L., 1988. High Temperature Creep Mechanisms in Single Crystals of Some High Performance Nickel Base Superalloys, in "High Temperature Alloys", J.B. Marriott et al Eds. Elsevier p. 9.
- Gao S., Rajendran M.K., Fivel M., Ma A., O. Shchyglo, Hartmaier A. and Steinbach I., 2015 a). Primary combination of phase-field and discrete dislocation dynamics methods for investigating athermal plastic deformation in various realistic Ni-base single crystal superalloy structures. *Mod. Simul. Mater. Sci. Eng.* **23(7)**, 075003.
- Gao S., Fivel M., Ma A. and Hartmaier A., 2015. b) Influence of misfit stresses on dislocation glide in single crystal superalloys: a 3D discrete dislocation dynamics study. *J. Mech. Phys. Solids* **76**, 276-290.
- Gao S., Fivel M. Ma A. and Hartmaier A., 2017. 3D discrete dislocation dynamics study of creep behavior in Ni-base single crystal superalloys by a combined dislocation climb and vacancy diffusion model. *J. Mech. Phys. Solids* **102**, 209-223.

- Hafez Haghghat S.M., Eggeler G., Raabe D. 2013. Effect of climb on dislocation mechanisms and creep rates in  $\gamma'$  strengthened Ni based superalloy single crystals: a discrete dislocation dynamics study. *Acta Mater.* **61**, 3709-3723.
- Hammer J. and Mughrabi H., 1989. High temperature creep and microstructure of the monocrystalline nickel base superalloy SRR 99. Proc. EUROMAT 89 European conference on advanced materials and processes, Aachen.
- Hardy M.C., Zirbel B., Shen G. and R. Shankar, 2004. Developing damage tolerance and creep resistance in a high strength nickel alloy for disc applications. In *Superalloys 2004*. Publisher TMS, the MMM Society, 83-90.
- Huang Z., Zhao L. and Tong J., 2012. DDD modeling of mechanical deformation of nickel based single crystal superalloys. *Int. J. Plast.* **28**, 141-158.
- Huang M. and Li Z., 2013. The key role of dislocation dissociation in the pastic behavior of single crystal nickel-based superalloy with low stacking fault energy: Three-dimensional discrete dislocation dynamics modelling. *J. Mec. Phys. Sol.* **61**, 2454-2472.
- Hussein A.M, Rao S.I., Uchic M.D., Parthasarathy T.A and El-Awady J.A, 2017. The strength and dislocation microstructure evolution in superalloy microcrystals, *J. Mech. Phys. Solids*, **99**, 146-162.
- Ichitsubo T., Koumoto D., Hirao M., Tanaka K, Osawa M., Yokokawa T. and Harada H., 2003. Rafting mechanism for Ni-base superalloy under external stress: elastic or elastic-plastic phenomena? *Acta Mater.*, **51**, 4033-4044.
- Knowles D.M. and Chen Q.Z.; 2003. Superlattice stacking fault formation and twinning during creep in  $\gamma$ - $\gamma'$  single crystal superalloy CMSX-4. *Mater. Sci. Eng. A* **340**, 88-102.
- Kubin L.P. 2013. Dislocations, mesoscale simulations and plastic flow, Oxford series on materials modelling, Oxford Materials.
- Kuhn H.-A., Biermann H., Ungár T. and Mughrabi H., 1991. An X-ray study of creep deformation induced changes of the lattice mismatch in the  $\gamma'$ -hardened monocrystalline Nickel base alloy SRR 99. *Acta Metall. Mater.* **39**, 2783-2794.
- Lasalmonie A. and Strudel J.L., 1975. Interfacial Dislocation Networks Surrounding  $\gamma'$  Precipitates in a Nickel Base Alloy. *Philos. Mag.* **32**, 937-949.
- Long H., Wei H., Liu Y., Mao S., Zhang J., Xiang S., Chen Y., Gui Y., Li Q., Zhang Z. and Han X., 2016. *Acta Mat.*, **120**, 95-107. Effect of lattice misfit on the evolution of the dislocation structure in Ni-based single crystal superalloys during thermal exposure.
- Louchet F., 1995. A model of negative creep in nickel based superalloys. *Scripta Metall. Mater.*, **33** (6), 913-918.
- Li R. and Wang Z., 2014. Parametric dislocation dynamics simulation of precipitation hardening in Ni-based superalloy. *Mater. Sci. Eng. A* **616**, 275-280.

- Link T., Epishin A. and Fedelich B., 2009. Inhomogeneity of misfit stresses in nickel-base superalloys: Effect on propagation of matrix dislocation loops. *Philos. Mag.* **89**, 1141-1159.
- Liu B., Raabe D., Roters F. and Arsenlis A., 2014. Interfacial dislocation motion and interactions in single-crystal superalloys. *Acta Mater.* **79**, 216-233.
- Lu Y., Ma S. and Majumdar B.S., 2008. Elastic microstrains during tension and creep of superalloys: results from *in situ* neutron diffraction. In *Superalloys 2008*. Ed. Reed R.C. et al. Publ. TMS, the MMM Society, 553-592.
- Matan N, Cox D.C., Rae C.M.F. and Reed R.C., 1989. On the kinetics of rafting in CMSX-4 superalloy single crystals. *Acta Mater.* **47**, 2031-2045
- Pineau A., 1976. Influence of uniaxial stress on the morphology of coherent precipitates during coarsening. Elastic energy considerations. *Acta Metall. Mater.* **24**, pp. 559-564.
- Pollock T.M. and Argon A.S., 1992. Creep resistance of CMSX-3 nickel base alloy single crystals. *Acta Metall. Mater.* **40**, 1-30.
- Pollock T.M. and Argon A.S., 1994. Directional coarsening in nickel base single crystals with high volume fractions of coherent precipitates. *Acta Metall. Mater.* **42**, 1859-1874.
- Pollock T.M. and Field R.D., 2002. Dislocations and high temperature deformation of superalloy single crystals in “Dislocations in Solids” Edit. F.R.N. Nabarro and M.S. Duesbery, *Elsevier Science*. Chapter 63, 547-618.
- Pope D.P. and Ezz S.S., 1984. Mechanical properties of Ni<sub>3</sub>Al and nickel-base alloys with high volume fraction of  $\gamma'$ . *Intl. Metals Rev.* **29**, 136.
- Preuss P., Da Fonseca J.Q., GRANT B., Knoche E., Moat R. and Daymond M., 2008. The effect of  $\gamma'$  particle size on the deformation mechanism in an advanced polycrystalline nickel-base superalloy. In *Superalloys 2008*. Ed. Reed R.C. et al. Publ. TMS, the MMM Society, 405-414.
- Provendier-Aubourg V. and Strudel J.L., 1995. Creep and relaxation mechanisms in a nickel base alloy at 650°C. *Phys. Stat. Sol. (a)* **149**, 355.
- Pyczak F., Devrient B., Neuner F.C. and Mughrabi H., 2005. The influence of different alloying elements on the development of  $\gamma$ - $\gamma'$  microstructures of nickel base superalloys during high temperature annealing and deformation. *Acta Mater.* **53**, 3879-3891.
- Pyczak F., Neumeier S. and Göken M., 2009. Influence of lattice misfit on the internal stress and strain states before and after creep investigated in nickel-base superalloys containing rhenium and ruthenium. *Mater. Sci. Eng.* **A510-511**, 295-300.
- Rae C.M.F. and Reed R.C., 2007. Primary creep in single crystal superalloys. Origin, mechanisms and effects. *Acta Mater.* **55**, 1067-1081.
- Rae C.M.F., Matan N. and Reed R.C., 2001. The role of stacking fault shear in the primary creep of [001] oriented single crystal superalloys at 750°C and 750 MPa. *Mater. Sci. Eng.* **A 300**, 125-134.

- Ram F., Li Z., Zaefferer S., Hafez Haghghat S.M., Zhu Z., Raabe D and Reed R.C., 2016. On the origin of creep dislocations in a Ni-base, single-crystal superalloy: an ECCI, EBSD, and dislocation dynamics-based study. *Acta Mater.* **109**, 151-161.
- Rao S. I., Parthasarathy T.A., Dimiduk T.A. and Hazzledine P.M., 2004. Discrete dislocation simulations of precipitation hardening in inverse superalloys. *Philos. Mag.* **86**, 215-225.
- Ratel N., Calderon H. A., Mori T. and Withers P. J., 2010. Predicting the onset of rafting of  $\gamma'$  precipitates by channel deformation in a Ni superalloys. *Philos. Mag.* **90**, 585-597.
- Ratel N., Bastie P., Moric T., and Withers P.J., 2009. Application of anisotropic inclusion theory to the energy evaluation for the matrix channel deformation and rafting geometry of Ni superalloys. *Mater. Sci. Eng. A* **505**, 41–47;
- Reed R.C., Matan N., Cox D.C. and Rae C.M.F., 1999. Creep of CMSX-4 superalloy single crystals: Effects of rafting at high temperature, *Acta Mater.* **47**, 367
- Reppich B., 1984. Negatives Kriechen. *Z. Metalkde*, **75**, 193-202.
- Royer A., Bastie P., Bellet D. and Strudel J.L., 1995. Temperature dependence of the lattice mismatch of the AM1 superalloy. Influence of the  $\gamma'$  precipitates morphology. *Philos. Mag.* **72**, 669-689.
- Schmidt R. and Fellerkniepmeier M., 1993. Phase chemistry of a nickel-base superalloy after creep experiments. *Scripta Metall. Mater.* **29**, 1079- 1084.
- Shin C.S., Fivel M., and Verdier K.H., 2003. On dislocation-impenetrable precipitates interactions: a discrete dislocation simulation analysis, *Phil. Mag.*, **83**(31-34), 3691-3704.
- Strudel J.L., 2007. Nickel base superalloys: an engineering and scientific challenge. In *Frontiers in the Design of Materials*. Edit. Baldev Raj, S. Ranganathan, S. Mannan, K Bhanu Sankara Rao, M.D. Mathew and P. Shankar. Series in Metallurgy and Materials Science. Universities Press Publisher in Hyderabad (India), 195-209.
- Svoboda J. and Lukáš P., 1998. Model of creep in  $\langle 001 \rangle$ -oriented superalloy single crystals. *Acta Mater.* **46**, 3421-3431.
- Tanaka K., Hashimoto W., Inoue T. and Inui H., 2011. Effect of elastic driving force on the evolution of microstructures in the secondary creep rate stage. *EuroSuperalloys 2006*. Advance Materials Research **278**, 126-131.
- Unocic R.R., Kovarik L., Shen C., Sarosi P.M., Wang Y., Li J., Ghosh S., and Mills M.J., 2008. In *Superalloys 2008*. Ed. Reed R.C. et al. Publ. TMS, the MMM Society, 377-385.
- Vattré A., B. Devincre and A. Roos, 2009. Dislocation dynamics simulations of precipitation hardening in Ni-based superalloys with high  $\gamma'$  volume fraction, *Intermetallics*, **17**, 988-994.
- Vattré A., Devincre B. and Roos A., 2010. Orientation dependence of plastic deformation in nickel-based single crystal superalloys: Discrete-continuous model simulations, *Acta Mater.* **58**, 1938-1951.

- Verdier M., Fivel M. and Groma I., 1998. Mesoscopic scale simulation of dislocation dynamic in fcc metals: Principle and applications. *Mod. Simul. Mater. Sci. Eng.* **6**, 755-770.
- Viswanathan G.B., Sarosi P.M., Whitis D.H. and Mills M.J., 2005. Deformation mechanisms at intermediate creep temperatures in the Ni-base superalloy René 88 DT. *Mater. Sci. Eng. A* **400-401**, 489-495.
- Weygand D., Friedman L.H., Van der Giessen E. and Needleman A., 2002. Aspects of boundary-value problem solutions with three-dimensional dislocation dynamics. *Int. J. Plast.* **10**, 437-468.
- Wu X., Wollgramm P., Somsen C., Dlouhy A., Kostka A. and Eggeler G., 2016. Double minimum creep of single crystal Ni-base superalloys. *Acta Mater.* **112**, 242-260.
- Yang H., Li Z. and Huang M., 2013. Modeling dislocation cutting the precipitate in nickel-based single crystal superalloy via the discrete dislocation dynamics with SISF dissociation scheme. *Comput. Mater. Sci.* **75**, 52-59.
- Yashiro K., Konishi M. and Tomita Y., 2008. Discrete dislocation dynamics study on the interaction between prismatic dislocation loop and interfacial network dislocations, *Comput. Mater. Sci.* **43**, 481-488.
- Yashiro K., Kurose F., Nakashima Y., Kubo K., Tomita Y. and Zbib H.M., 2006. Discrete dislocation dynamics simulation of cutting of  $\gamma'$  precipitate and interfacial dislocation network in Ni-based superalloys. *Int. J. Plast.* **22**, 713-723.
- Zalezak T., Svoboda J. and Dlouhy A., 2017. High temperature dislocation processes in precipitation hardened crystals investigated by 3D discrete dislocation dynamics. *Int. J. Plast.* **97**, 1-23.
- Zbib H.M., Diaz de la Rubia T., 2002. A multiscale model of plasticity. *Int. J. Plast.* **18**, 1133-1163.
- Zhang J.X., Wang J.C., Harada H. and Koizumi Y., 2005. The effect of lattice misfit on the dislocation motion in superalloys during high-temperature low-stress creep. *Acta Mater.* **53**, 4623-4633.
- Zhang J.X., Harada H., Koizumi Y. and Kobayashi T., 2010. Dislocation motion in the early stage of high temperature low stress creep in a single crystal superalloy with a small lattice misfit. *J. Mater. Sci.* **45**, 523-532.